



**AFRL-OSR-VA-TR-2015-0072**

---

(YIP 11) Morphing Carbon Nanotube Microstructures

**Wei Lu**  
**UNIVERSITY OF MICHIGAN**

---

**02/20/2015**  
**Final Report**

<p><b>DISTRIBUTION A: Distribution approved for public release.</b></p>
---

Air Force Research Laboratory  
AF Office Of Scientific Research (AFOSR)/RTD  
Arlington, Virginia 22203  
Air Force Materiel Command

<b>REPORT DOCUMENTATION PAGE</b>				Form Approved OMB No. 0704-0188	
<p>The public reporting burden for this collection of information is estimated to average 1 hour per response, including the time for reviewing instructions, searching existing data sources, gathering and maintaining the data needed, and completing and reviewing the collection of information. Send comments regarding this burden estimate or any other aspect of this collection of information, including suggestions for reducing the burden, to Department of Defense, Executive Services, Directorate (0704-0188). Respondents should be aware that notwithstanding any other provision of law, no person shall be subject to any penalty for failing to comply with a collection of information if it does not display a currently valid OMB control number.</p> <p>PLEASE DO NOT RETURN YOUR FORM TO THE ABOVE ORGANIZATION.</p>					
<b>1. REPORT DATE (DD-MM-YYYY)</b> 20-03-2015		<b>2. REPORT TYPE</b> Final Performance		<b>3. DATES COVERED (From - To)</b> 01-06-2011 to 31-08-2014	
<b>4. TITLE AND SUBTITLE</b> Morphing Carbon Nanotube Microstructures				<b>5a. CONTRACT NUMBER</b>	
				<b>5b. GRANT NUMBER</b> FA9550-11-1-0089	
				<b>5c. PROGRAM ELEMENT NUMBER</b>	
<b>6. AUTHOR(S)</b> Wei Lu, Anastasios Hart				<b>5d. PROJECT NUMBER</b>	
				<b>5e. TASK NUMBER</b>	
				<b>5f. WORK UNIT NUMBER</b>	
<b>7. PERFORMING ORGANIZATION NAME(S) AND ADDRESS(ES)</b> UNIVERSITY OF MICHIGAN 503 THOMPSON ST ANN ARBOR, MI 48109-1340 US				<b>8. PERFORMING ORGANIZATION REPORT NUMBER</b>	
<b>9. SPONSORING/MONITORING AGENCY NAME(S) AND ADDRESS(ES)</b> AF Office of Scientific Research 875 N. Randolph St. Room 3112 Arlington, VA 22203				<b>10. SPONSOR/MONITOR'S ACRONYM(S)</b> AFOSR	
				<b>11. SPONSOR/MONITOR'S REPORT NUMBER(S)</b>	
<b>12. DISTRIBUTION/AVAILABILITY STATEMENT</b> A DISTRIBUTION UNLIMITED: PB Public Release					
<b>13. SUPPLEMENTARY NOTES</b>					
<b>14. ABSTRACT</b> <p>This AFOSR YIP Program sought to investigate the fabrication and properties of 3D morphing carbon nanotube (CNT) microstructures. It was proposed that morphing CNT microstructures would operate by swelling of an active material in a direction locally perpendicular to the CNTs. This shape change, in combination with the mechanical and electrical characteristics of the CNTs, could enable incorporation of intrinsic actuation and sensing behaviors in design of new structural materials and active surfaces.</p>					
<b>15. SUBJECT TERMS</b> <p>Morphing Structures, Plant-mimetic Design, Carbon Nanotube, Active Polymers</p>					
<b>16. SECURITY CLASSIFICATION OF:</b>			<b>17. LIMITATION OF ABSTRACT</b>	<b>18. NUMBER OF PAGES</b>	<b>19a. NAME OF RESPONSIBLE PERSON</b> Wei Lu
<b>a. REPORT</b>	<b>b. ABSTRACT</b>	<b>c. THIS PAGE</b>			<b>19b. TELEPHONE NUMBER (Include area code)</b> 734- 615-2306
U	U	U	UU		

## YIP: Morphing Carbon Nanotube Microstructures (FA9550-11-1-0089)

Final Performance Report

PI: A. John Hart (University of Michigan, MIT), [ajhart@mit.edu](mailto:ajhart@mit.edu)

This AFOSR YIP Program sought to investigate the fabrication and properties of 3D “morphing” carbon nanotube (CNT) microstructures. This concept was inspired by the design and responsive behavior of plant tissues that swell or contract in response to a stimulus, and it was proposed that morphing CNT microstructures would operate by swelling of an active material in a direction locally perpendicular to the CNTs (Fig. 1). This shape change, in combination with the mechanical and electrical characteristics of the CNTs, could enable incorporation of intrinsic actuation and sensing behaviors in design of new structural materials and active surfaces.

This final performance report, presented in four self-contained chapters, describes the major accomplishments of the AFOSR program. These include advances in the fabrication and mechanics of CNT microstructures, and demonstrations of novel composite materials and active materials based on composites of organized CNTs, polymers, and ceramics. The chapters are:

- **1: Corrugated paraffin nanocomposite films as large stroke thermal actuators and self-activating thermal interfaces.** We demonstrate that compact, high-performance paraffin actuators can be made by confining paraffin within vertically aligned carbon nanotube films. This large-stroke vertical actuation is enabled by strong capillary interaction between paraffin and CNTs and by engineering the CNT morphology by pre-compression before capillary-driven infiltration of the molten paraffin. The maximum actuation strain ( $\sim 0.02$ - $0.2$ ) approaches that of natural muscle and exceeds that of shape memory alloys. Further, we show how a CNT-paraffin film can serve as a self-activating thermal interface that closes a gap when it is heated. These new CNT-paraffin film actuators could be scaled to large-area production and lamination, and are attractive for practical use in miniature systems due to their self-contained design.
- **2: Replica molding of liquid crystal network (LCN) polymer microstructures for active surfaces.** We present a replica molding (RM) fabrication technique to obtain high fidelity surface bound glassy LCN microstructure actuators over large areas. The removal of oxygen during curing was critical to achieve high-fidelity replicas with smooth surface texture, while the necessary LCN alignment for actuation was obtained via curing in a magnetic field. Cast microstructures had lateral dimensions of a few microns and aspect ratios (AR) up to 15:1. A gradient based edge detection algorithm was used to quantify the LCN microstructure actuation, verifying anisotropy of the network.
- **3: Strain-engineered manufacturing of freeform carbon nanotube microstructures.** Here, we demonstrate a new technique for scalable manufacturing of freeform microstructures, via strain-engineered growth of aligned carbon nanotubes (CNTs). Offset patterning of the CNT growth catalyst is used to locally modulate the CNT growth rate. This causes the CNTs to collectively bend during growth, with exceptional uniformity over large areas. The final shape of the curved CNT microstructures can be designed via finite element modeling, and compound catalyst shapes produce microstructures with multi-directional curvature and unusual self-organized patterns. Conformal coating of the CNTs enables tuning of the mechanical properties

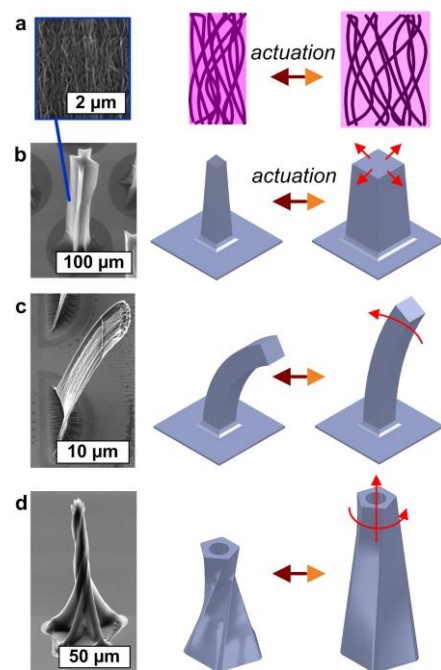


**Fig. 1.** Morphing CNT microstructure concept: (a) lateral swelling of aligned CNT network; (b) radial expanding actuator; (c) lateral bending actuator; (d) vertical twisting actuator.

independently from the microstructure geometry, representing a versatile principle for design and manufacturing of complex microstructured surfaces.

- **4: Scaling the stiffness, strength, and toughness of ceramic-coated nanotube foams into the structural regime.** We demonstrate how to use aligned carbon nanotube (CNT) growth followed by atomic layer deposition (ALD) to manufacture nanocomposite foams with precisely controllable mechanical properties. By starting with a low density CNT forest and varying the ALD coating thickness, we realize predictable  $\sim 1000$ -fold control of Young's modulus (14 MPa to 20 GPa, where  $E \sim \rho^{2.8}$ ), ultimate compressive strength (0.8 MPa to 0.16 GPa), and energy absorption (0.4 to 400 J/cm<sup>3</sup>). Owing to the continuous, long CNTs within the ceramic nanocomposite, the compressive strength and toughness of the foam are 10-fold greater than commercially available aluminum foam over the same density range. Moreover, the compressive stiffness and strength equal that of compact bone at 10% lower density. Along with emerging technologies for scalable patterning and roll-to-roll manufacturing and lamination of CNT films, coated CNT foams may enable new materials for mechanical and multifunctional applications such as catalysis, filtration, and thermal protection.

Future work may focus on achieving extreme stimuli-responsive deformations using CNT-polymer and CNT-LCN systems, and enabling multifunctional surfaces combining the strain-dependent electrical properties of CNTs with their active response.

## Chapter 1: Corrugated paraffin nanocomposite films as large stroke thermal actuators and self-activating thermal interfaces

*Contents of this chapter have been submitted for publication as: D. Copic and A.J. Hart, "Corrugated paraffin nanocomposite films as large stroke thermal actuators and self-activating thermal interfaces."*

### Introduction

The development of active materials whose dimensions can be changed using externally applied electrical, optical, or thermal stimuli, is essential to advances in actuators for use in miniaturized grippers and pumps, probes for scanning probe microscopy, and ultrasonic transducers. Specifically, paraffin wax has found longstanding use in linear actuators with centimeter-scale and larger dimensions, which are widely used in automotive and aerospace systems. This is because paraffin wax exhibits a large and repeatable volume change (10-40%) and stress output (10 – 100 MPa)<sup>1,2</sup> upon melting, resulting in a high mechanical energy density ( $10^7 \text{ J m}^{-3}$ )<sup>2</sup> (Figure S1). In comparison to paraffin, thin film shape memory alloy (SMA) actuators exhibit actuations strains of  $7 \times 10^{-3} - 7 \times 10^{-2}$  and stresses of 100 – 700 MPa, while thin film piezoelectric (PZT) actuators exhibit actuation strains of  $5 \times 10^{-6} - 2 \times 10^{-4}$  and stresses of 1 – 9 MPa<sup>3</sup>.

Paraffin has also been incorporated in micro-scale systems including on-chip pumps<sup>4</sup>, valves<sup>5-8</sup>, thin-film cantilevers<sup>5,9</sup>, and linear actuators<sup>10</sup>. These designs and the related fabrication methods are complicated by the need to confine the paraffin during melting, which is needed to convert the expansion of the paraffin wax into a directed motion. As a result, the overall system performance of miniature paraffin actuators is often compromised relative to the intrinsic actuation capability of paraffin, and these actuators require a large footprint compared to the size of active material used.

Therefore, owing to its intrinsic performance and simplicity of operation, it would be useful to develop more scalable means to harness the actuation capability of paraffin wax in composite materials. Recently, Lima et al. demonstrated micro-fiber actuators comprised of carbon nanotube (CNT) yarns infiltrated with paraffin wax<sup>11,12</sup>. In these actuators, the wax melts inside the yarn upon heating, and remains confined within the yarn due to its strong wetting of the CNTs and high surface tension. As the wax expands, it swells the CNT yarn, causing the

composite to contract its length due to the mechanical anisotropy introduced by the twist of the CNTs about the yarn axis. These yarns exhibited up to 8% contraction upon heating<sup>11</sup> and were able to lift 17,700 times their own weight with a 3% contraction.

Here, we show how large stroke thin film nanocomposite actuators can be made by confining paraffin within vertically aligned CNT films (CNT “forests”) and how the actuation stroke of the composite can be engineered by corrugating the forests. Via this strategy, we demonstrate the fabrication of large-stroke CNT-paraffin composite film actuators, and show that the actuation performance is governed by two distinct mechanistic regimes of operation: (1) low strain expansion below the wax melting point, wherein the composite actuator has high stiffness and (2) high strain expansion during and beyond the melting transition, wherein the actuator has much lower stiffness. Last, we show how the high strain regime can be exploited to build a self-activating thermal interface, where the vertical extension of the nanocomposite film causes it to contact a second substrate, resulting in enhanced heat dissipation at elevated temperature.

## Methods

*CNT growth:* CNT forests were grown using chemical vapor deposition (CVD) from a thin film catalyst (1 nm Fe supported on 10 nm Al<sub>2</sub>O<sub>3</sub>), which was sputtered on a (100) Si wafer coated with 300 nm thermally grown SiO<sub>2</sub>. The wafer was cut into 4 mm by 8 mm chips using a dicing saw. Two chips were placed side-by-side inside a horizontal tube furnace (Scientific Mini-Mite) at atmospheric pressure., which was then flushed with helium, heated in a 400:100 sccm H<sub>2</sub>:He gas mixture for 10 minutes to 775°C, annealed, held under these conditions for a further 10 minutes, and exposed to a 100:400:100 sccm H<sub>2</sub>:He:C<sub>2</sub>H<sub>4</sub> gas mixture for 20-22 minutes for CNT growth. Rapid cooling of the CNT forests was achieved by shifting the quartz tube downstream until the CNT forests were outside the furnace.

*Paraffin wax infiltration:* CNT forests were inverted such that their top made contact with a 2cm by 2cm silicon chip, which was heated to 100°C by a hotplate. The forests were then compressed by 10-50% of its initial height using a vertical precision actuator. While maintaining the position and temperature, molten paraffin wax was added to the silicon chip and promptly wicked into the CNT forest. Constant load was applied during sample cooling and the sample was manually separated from the silicon chip. The sample was then placed on a spin coater and exposed it to

75mW/cm<sup>2</sup> of ultra violet (UV) light (Dymax Model 2000) for 35s prior to spinning. Excess paraffin was then spun away at 3000 rpm for 30 seconds while the UV light was maintained.

*Displacement and load measurements:* All forest indentation, displacement, and force measurements under load were collected using a custom-built single axis precision actuator with both PID position and load control. The custom precision actuator was driven by a voice coil, while the actuator motion was measured using an optical encoder and the load was measured using a S-beam load cell (Futek). The actuator displacement under no load was obtained by an edge-tracking algorithm, which was used on a series of high-resolution images taken by a telecentric lens of the actuator side view backlit by a collimated white light source.

*Thermal conductivity measurement:* CNT-paraffin actuators were placed on a PI controlled hotplate (Torrey Pines Scientific HS40) instrumented with a heat flux sensor and thermocouple (Omega HFS-4), while a similarly instrumented heat sink was separated from the actuator by 100μm using a micrometer stage. The temperature of the hotplate was slowly ramped from room temperature to 80°C while recording the heat fluxes and temperatures. Displacement measurements were obtained using the edge tracking algorithm and setup described above. The thermal resistivity was calculated using the measured data and a simple thermal network resistance model, which accounted for the convective heat transfer between the heat source and sink, the thermal contact resistance, and the resistance of the silicon substrate and air gap.

## **Results and Discussion**

CNT-paraffin nanocomposite films were fabricated by capillary driven infiltration of molten paraffin wax into vertically aligned CNT forests, as shown in Figure 1. First, CNT forests were grown on silicon wafers by atmospheric pressure thermal chemical vapor deposition (CVD) using a supported catalyst (1/10 nm Fe/Al<sub>2</sub>O<sub>3</sub>) deposited by sputtering (see Methods)<sup>13,14</sup>. After the allotted growth time, which determines the CNT forest height, the CVD system was cooled rapidly while maintaining the hydrocarbon flow; this resulted in strong CNT-substrate adhesion, which prevented delamination of the forest during paraffin expansion.

Next, the CNT forest was compressed vertically using a precision actuator, while resting on a hot plate. Upon compression the CNTs collectively folded, starting at the base of the forest, resulting in the corrugated morphology shown in Figure 1D<sup>15–18</sup>. The corrugated morphology is visually reminiscent of a macroscopic accordion bellows. Unless otherwise noted below, the

CNT forest was compressed to 50% of its as-grown height. Next, the corrugated CNT forest was heated to 100°C and molten paraffin wax was poured onto the sample from the side, while maintaining the compressive load. The wax rapidly wetted the CNTs and wicked into the forest. The hot plate was then cooled ( $\sim 4^{\circ}\text{C}/\text{min}$ ) to 35°C while keeping the sample under constant load. Last, the wax-infiltrated CNT forest was removed from the hot plate, and placed on a spin-coater. The sample was heated using a UV lamp, which caused the wax to melt, and spinning was used to remove excess wax from the substrate while retaining wax within the CNT forest due to capillary action.

The corrugated forest morphology is essential to achieving large actuation stroke upon paraffin phase change. Maintaining compressive load during paraffin infiltration and cooling allows the corrugated morphology to be maintained in the nanocomposite film. If the CNT forest is unloaded before paraffin infiltration, the wave-like corrugation is only partially recovered because the elastic energy stored in the deformed CNTs is counteracted by the van der Waals adhesion between CNT contacts created during forest compression. If the forest is infiltrated with paraffin without maintaining the compressive load, the forest expands to approximately 80% of its initial height during cooling and develops cracks in its top surface during cooling (Figure S2). These cracks, which extend through to the substrate, are caused by local capillary aggregation of the CNTs, which is driven by the shrinkage of the wax upon cooling. The pressure from capillary aggregation exceeds the lateral strength of the forest and causes these cracks. Upon thermal cycling, such cracked composite films close and open their cracks, instead of expanding and contracting vertically, and therefore do not operate as intended.

Upon heating, the crack-free nanocomposite film expands vertically and the wavelength of the corrugations increases, visually resembling inflation of an accordion bellows. A side view optical image at 25°C and a mirrored image of the same film heated to 150°C are shown in Figure 2A. Measurements of the thermally induced strain with no load applied were made via edge tracking of optical images taken using a telecentric lens backlit by a collimated white light source. This actuator extended vertically by  $\sim 17\%$  (perpendicular to the substrate) at 150°C, as shown in Video S3. Strain versus temperature data from three consecutive heating and cooling cycles (Figure 2B) shows that the vertical actuation of the nanocomposite is repeatable.

With increasing temperature below the melting point, the CNT-paraffin film expands slowly, then it expands rapidly through the melting transition (53-57°C), and after that it expands in an



approximately linear relationship with temperature. Thus, the strain-temperature curve of a characteristic CNT-paraffin actuator has three distinct regions: (1) low thermal expansion below the melting point, (2) rapid expansion during melting, and (3) further expansion driven by the increased pressure of the confined molten wax. In the second and third regions, the shape of the curve for the CNT-paraffin nanocomposite is similar to that for unconstrained paraffin wax of similar molecular weight<sup>19</sup>, but exhibits a lower volume change. Through the complete thermal cycle, the CNT-paraffin films undergo a volume change of approximately 20%, compared to approximately 40% expected for unconstrained neat paraffin with similar molecular weight. The observed volume change is reduced because the paraffin must work against the stiffness of the CNT forest to expand the composite. Comparable mechanisms limit the strain of macroscale paraffin actuators, yet to a smaller degree, wherein the paraffin is held within a container. For further discussion, we denote the low thermal expansion region below the melting point as “regime 1” and the subsequent behavior of rapid expansion upon melting and linear expansion beyond melting as “regime 2”.

To explore the relationship between applied force and actuation strain, we applied constant loads during heating while monitoring the vertical displacement of the film, using a feedback-controlled loading system. Consecutive thermal strain curves under constant stress levels varying by factors of ten, from 0.01 kPa to 10 kPa, are shown in Figure 2C. In regime 1 (below the wax melting point), all four strain curves overlap closely and reach a maximum thermal strain of 3% at 50°C. For all but the 10kPa curve, rapid expansion upon melting takes place. As expected, an increase in applied load leads to smaller actuation strains. At 10kPa load, the CNT-paraffin nanocomposite collapses after melting, suggesting that the blocking stress of the CNT-paraffin actuator in regime 2 (above the wax melting point) is between 1-10kPa. In the data shown, the strains reached under load surpass those reached in the no load condition, which is likely due to run-to-run variation in CNT forest density<sup>20</sup>.

Once the wax is melted inside the CNT forest (>60°C), the vertical stiffness of the film decreases significantly, as shown in Figure 3. This signifies the onset of regime 2. At room temperature the modulus of the actuator is 18.6 MPa, which is approximately 15-fold greater than a corrugated (crushed) CNT forest that has not been infiltrated with paraffin. The actuator stiffness unexpectedly increases to 46.7 MPa at 40°C. The actuator stiffness then drops

significantly, to 4.5MPa, as the wax melts at 60°C, while at 100°C the stiffness of the actuator drops to 1.2 MPa, which is less than the stiffness of the corrugated CNTs without paraffin.

In regime 1, actuation of the CNT-paraffin film is powered by the release of the deformation energy (stored in the CNTs during wax freezing), which does work against the viscous forces in the wax and lifts the applied load upwards by up to 3% strain at 10kPa. Because the compressive load used to crush the forest is maintained during cooling of the freshly infiltrated wax, and because wax undergoes shrinkage during cooling, additional elastic energy is stored in the CNT network during freezing of the wax. As the wax softens before melting, it allows the corrugated microstructure to relax, releasing the stored deformation energy. When the wax melts, the wavelength of the corrugated CNT morphology increases, signaling the onset of regime 2. The behavior of the composite in regime 1, below the wax melting point, is analogous to shape memory materials, where potential energy is first stored during cooling and is later released during heating, resulting in a shape change. However, unlike most shape memory materials, upon cooling the wax pulls the CNTs back to their original shape, without requiring an external restoring force. Therefore, the CNT-paraffin system is a fully reversible shape memory composite, and to our knowledge this is the first time that such has been achieved using paraffin wax as the active material.

In regime 2, the wax has undergone melting and expands up to 20% more in total, doing work to extend the corrugated CNT forest. The equilibrium position of the actuator, at elevated temperature, is reached when pressure of the molten wax inside the forest equals the pressure required to incrementally extend the forest in the vertical direction in addition to any externally applied load. If the pressure exerted by the paraffin exceeds the capillary pressure, the molten wax is expected to flow out of the forest. For example, loading an actuator to 100kPa at 150°C results in the escape of wax and the film becomes compressed to less than 10% of its initial height.

The actuation properties of CNT-paraffin films are strongly dependent on the compression strain applied to the CNT forest before and during paraffin infiltration; we found that samples compressed by approximately 50% of their initial height resulted in the actuators with the largest vertical stroke (Figure S4). When compressed by 50% of its as-grown thickness, a CNT forest was observed to have a corrugated conformation for the lower 45-50% of its compressed thickness (as viewed from the side). Further, the density and alignment of the CNTs within the

forest are expected to influence the capillary pressure confining the wax within the composite, therefore changing the actuator stiffness and strain output. A greater CNT density would result in a lower average spacing between individual CNTs, resulting in a greater capillary pressure of the paraffin and therefore a greater blocking stress of the actuator. Additionally, we expect a greater CNT forest density will correspond to greater actuator stiffness at the expense of less maximum strain. For regime 2, this tradeoff is due to the energy density of the process powering the shape change, in this case the phase transition and thermal expansion of paraffin, remaining largely unchanged by the density, morphology, or increased stiffness of the CNT forests.

While the CNT-paraffin actuators exert a relatively low stress after melting ( $<10\text{kPa}$ ), the maximum actuation strain ( $\sim 0.02\text{-}0.2$ ) approaches that of natural muscle ( $\sim 0.3\text{-}0.7$ ) and exceeds that of shape memory alloys ( $\sim 0.07$ ). Further study is needed to explore the mechanism and limits of actuation, yet it is clear that the strain and stress will be related to the density of the CNTs, their initial deformation, and the intrinsic active behavior of the paraffin wax. Moreover, although the blocking stress for regime 1 is not known, the present CNT-paraffin film actuator is able to lift at least 2,000 times its weight at  $100^\circ\text{C}$ . A comparison of the CNT-paraffin film performance to traditional actuators and active materials can be found in Figure S6.

Last, we explore one potential application of the CNT-paraffin film actuator, a passive thermal switch<sup>21</sup>, which enables engineered heat dissipation via self-actuated contact with a second surface. We present a preliminary demonstration of this by measuring the thermal conductivity of the CNT-paraffin actuator as it expands upward to contact a second surface. We constructed a setup with thin film heat flux sensors on parallel surfaces (Figure 4A), and the measured heat flux through the composite versus temperature as it closes the gap between the surfaces (Figure 4B). The thermal conductivity of the CNT-paraffin composite was calculated from a combined thermal resistance model using the measured heat flux into the heat sink and the temperature difference between the hotplate and the heat sink (see SI for model description).

When the system is heated from below the CNT-paraffin film, the thermal resistance is initially large while most of the heat is absorbed by the paraffin wax. As the film expands, the thermal resistance of the actuator and the gap decreases rapidly, the air gap is reduced, the conductivity of the paraffin increases<sup>22</sup>, and ultimately the actuator contacts the heat sink. As the gap closes and the composite contacts the upper heat sink, the thermal conductivity increases to approximately  $0.4\text{ W/m-K}$  at  $70^\circ\text{C}$  (Figure S5). This is approximately twice that of neat

paraffin (0.21–0.24 W/m-K). The greater thermal conductivity than neat paraffin is due to the presence of aligned CNTs within the composite (~1 wt%). The final value is comparable to commercially available polymer-ceramic composite thermal transfer tapes<sup>23</sup>, and is close to that of passive composites made by polymer infiltration to CNT forests<sup>24,25</sup>. In principle, the temperature at which the actuator engages the heat sink could be controlled via the initial gap or the physical characteristics of the CNT-paraffin film (pre-strain, paraffin composition, CNT density, etc.).

## **Conclusion**

In conclusion, we have shown that large-stroke thermal actuators can be made by infiltration of corrugated CNT forests with paraffin wax. Two mechanistic regimes of the CNT-paraffin actuator were identified: (1) a high stiffness, low strain regime below the melting point, which is analogous to the performance of shape memory materials and (2) a low stiffness, high strain regime above the melting point. In regime 1 the actuator was capable of lifting 2,000 times its own weight with an actuation strain of 3% and a stress of 10kPa at 40°C, while in regime 2 the actuator was shown to reach an actuation strain of 20% and a stress of 1kPa at 175°C. This large-stroke vertical actuation is enabled by strong capillary interaction between paraffin and CNTs, and engineering of the vertical compliance by corrugation of the CNT forest. CNT-paraffin nanocomposites have been shown to act as switchable thermal interfaces with a thermal conductivity up to 0.4 W/m-K at 70°C with a CNT content of 1 wt%. Because the CNT-paraffin film actuators do not require external confinement to restrain the wax, the materials are amenable to integration with laminates and miniaturization for applications including thermal switching and flow control.

## **Acknowledgements**

Primary financial support was provided by the Air Force Office of Scientific Research Young Investigator Program (FA9550-11-1-0089). The force control system and imaging apparatus was originally built for a project funded by the Department of Energy Office of Basic Energy Sciences (DE-SC0004927). We thank Justin Beroz, Mostafa Bedewy, Kendall Teichert, Ryan Oliver, and Tom Serbowicz for contributions to the design and fabrication of the force control and imaging systems. Microfabrication was performed at the Lurie Nanofabrication Facility

(LNF), which is a member of the National Nanotechnology Infrastructure Network (NNIN), and electron microscopy was performed at the Electron Microbeam Analysis Laboratory (EMAL), both at the University of Michigan.

## References

1. Kabei, N. *et al.* A Thermal-Expansion-Type Microactuator with Paraffin as the Expansive Material : Basic Performance of a Prototype Linear Actuator. *JSME Int. J. Ser. C* **40**, 736–742 (1997).
2. Carlen, E. T. & Mastrangelo, C. H. Electrothermally activated paraffin microactuators. *J. Microelectromechanical Syst.* **11**, 165–174 (2002).
3. Huber, J. E., Fleck, N. A. & Ashby, M. F. The selection of mechanical actuators. *Proc. R. Soc. London. Ser. A Math. Phys. Eng. Sci.* **453**, 2185–2205 (1997).
4. Bodén, R. *et al.* A polymeric paraffin actuated high-pressure micropump. *Sensors Actuators A Phys.* **127**, 88–93 (2006).
5. Selvaganapathy, P., Carlen, E. T. & Mastrangelo, C. H. Electrothermally actuated inline microfluidic valve. *Sensors Actuators A Phys.* **104**, 275–282 (2003).
6. Carlen, E. T., Edwin, T. & Mastrangelo, C. H. C. H. Surface micromachined paraffin-actuated microvalve. *J. Microelectromechanical Syst.* **11**, 408–420 (2002).
7. Boustheen, A., Homburg, F. G. A., Somhorst, M. G. A. M. & Dietzel, A. A layered modular polymeric  $\mu$ -valve suitable for lab-on-foil: design, fabrication, and characterization. *Microfluid. Nanofluidics* **11**, 663–673 (2011).
8. Yang, B. & Lin, Q. A latchable microvalve using phase change of paraffin wax. *Sensors Actuators A Phys.* **134**, 194–200 (2007).
9. Thornell, L. K. and G. A thermal microactuator made by partial impregnation of polyimide with paraffin. *J. Micromechanics Microengineering* **12**, 849 (2002).
10. Lehto, M., Bodén, R. & Simu, U. A polymeric paraffin microactuator. *J. Microelectromechanical Syst.* **17**, 1172–1177 (2008).
11. Lima, M. D. *et al.* Electrically, chemically, and photonicallly powered torsional and tensile actuation of hybrid carbon nanotube yarn muscles. *Science* **338**, 928–32 (2012).
12. Chun, K.-Y. *et al.* Hybrid carbon nanotube yarn artificial muscle inspired by spider dragline silk. *Nat. Commun.* **5**, 3322 (2014).
13. Hart, A. J. & Slocum, A. H. Rapid Growth and Flow-Mediated Nucleation of Millimeter-Scale Aligned Carbon Nanotube Structures from a Thin-Film Catalyst. *J. Phys. Chem. B* **110**, 8250–8257 (2006).
14. Copic, D., Park, S. J., Tawfick, S., De Volder, M. & Hart, A. J. Fabrication, Densification, and Replica Molding of 3D Carbon Nanotube Microstructures. *J. Vis. Exp.* (2012).

15. Cao, A., Dickrell, P. L., Sawyer, W. G., Ghasemi-Nejhad, M. N. & Ajayan, P. M. Super-compressible foamlike carbon nanotube films. *Science* **310**, 1307–10 (2005).
16. Hutchens, S. B., Needleman, A. & Greer, J. R. A microstructurally motivated description of the deformation of vertically aligned carbon nanotube structures. *Appl. Phys. Lett.* **100**, 121910 (2012).
17. Pour Shahid Saeed Abadi, P., Hutchens, S. B., Greer, J. R., Cola, B. a. & Graham, S. Buckling-driven delamination of carbon nanotube forests. *Appl. Phys. Lett.* **102**, 223103 (2013).
18. Pathak, S. *et al.* Failure and Strength in Vertically Aligned Carbon Nanotubes. *ACS Nano* **7**, 8593–8604 (2013).
19. Simha, R., Wilson, P. & Olabisi, O. Pressure-volume-temperature properties of amorphous polymers: empirical and theoretical predictions. *Kolloid-Z. u. Z. Polym.* **251**, 402–408 (1973).
20. Oliver, C. R. *et al.* Statistical analysis of variation in laboratory growth of carbon nanotube forests and recommendations for improved consistency. *ACS Nano* **7**, 3565–80 (2013).
21. Geng, X., Patel, P., Narain, A. & Meng, D. D. A self-adaptive thermal switch array for rapid temperature stabilization under various thermal power inputs. *J. Micromechanics Microengineering* **21**, 085018 (2011).
22. Sarı, A. & Karaipekli, A. Thermal conductivity and latent heat thermal energy storage characteristics of paraffin/expanded graphite composite as phase change material. *Appl. Therm. Eng.* **27**, 1271–1277 (2007).
23. 3M™. *Thermally Conductive Adhesive Transfer Tapes 8805 • 8810 • 8815 • 8820*. (2008). at [http://multimedia.3m.com/mws/mediawebserver?mwsId=SSSSSuH8gc7nZxtU4x2v4x\\_GevUqe9Uz7vTSevTSeSSSSSS--&fn=78690099987.PDF](http://multimedia.3m.com/mws/mediawebserver?mwsId=SSSSSuH8gc7nZxtU4x2v4x_GevUqe9Uz7vTSevTSeSSSSSS--&fn=78690099987.PDF)
24. Marconnet, A. M., Yamamoto, N., Panzer, M. a, Wardle, B. L. & Goodson, K. E. Thermal conduction in aligned carbon nanotube-polymer nanocomposites with high packing density. *ACS Nano* **5**, 4818–25 (2011).
25. Cola, B. A., Hodson, S. L., Xu, X. & Fisher, T. S. Carbon Nanotube Array Thermal Interfaces Enhanced With Paraffin Wax. in *ASME 2008 Heat Transf. Summer Conf.* 765–770 (2008).

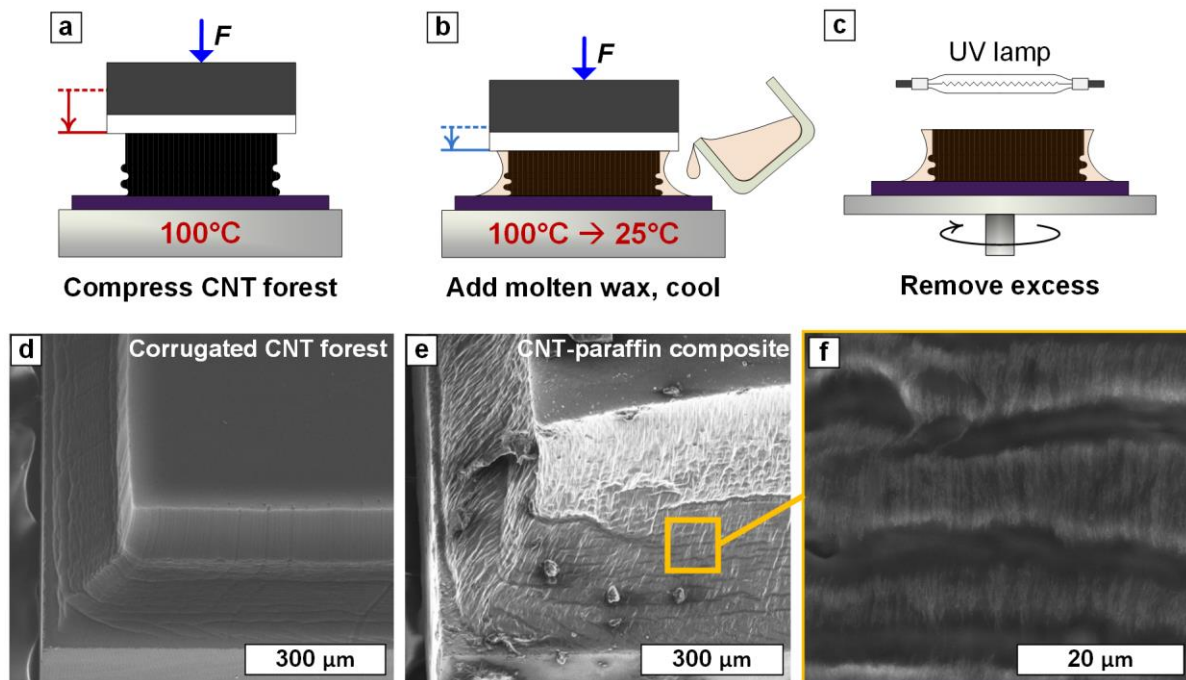


Figure 1. Fabrication of corrugated CNT-paraffin nanocomposite films: (a-c) Key process steps; SEM images of (d) compressed CNT forest with corrugations and (e) CNT-paraffin composite film, with (f) close-up of corrugated microstructure.



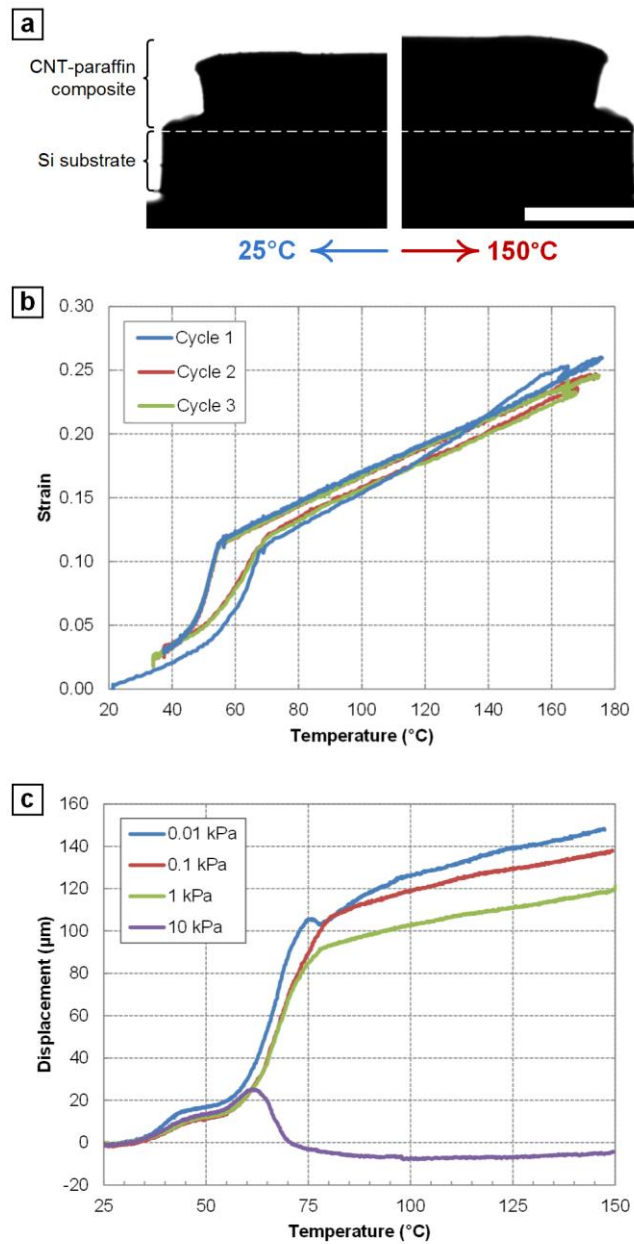


Figure 2. Actuation of CNT-paraffin composite films: (a) Image of the actuator side view at 25 $^{\circ}\text{C}$  and a mirrored image of the same view at 150 $^{\circ}\text{C}$  with 1mm scale bar. (b) Three consecutive cycles of a CNT-paraffin actuator under no load. (c) Displacement and strain versus temperature under varying values of constant applied stress during heating.

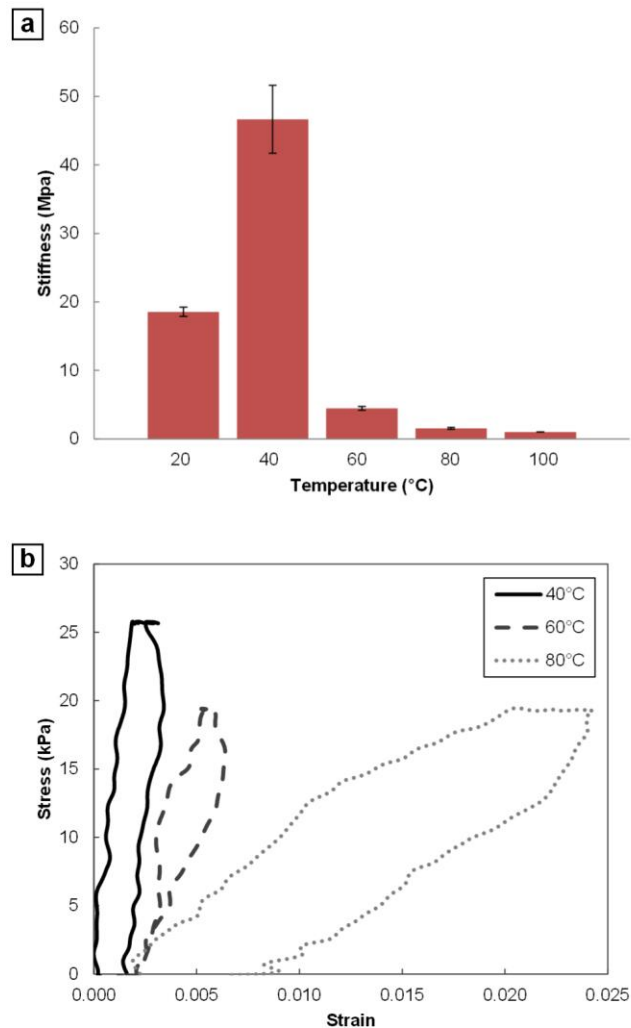


Figure 3. (a) Temperature dependent compressive stiffness of CNT-paraffin films and (b) exemplary stress-strain curves used to determine stiffness.

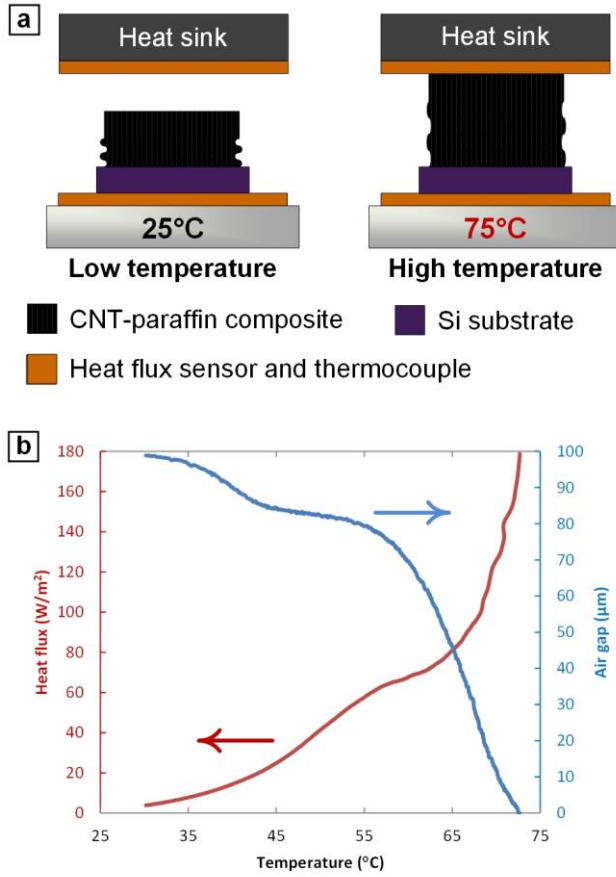
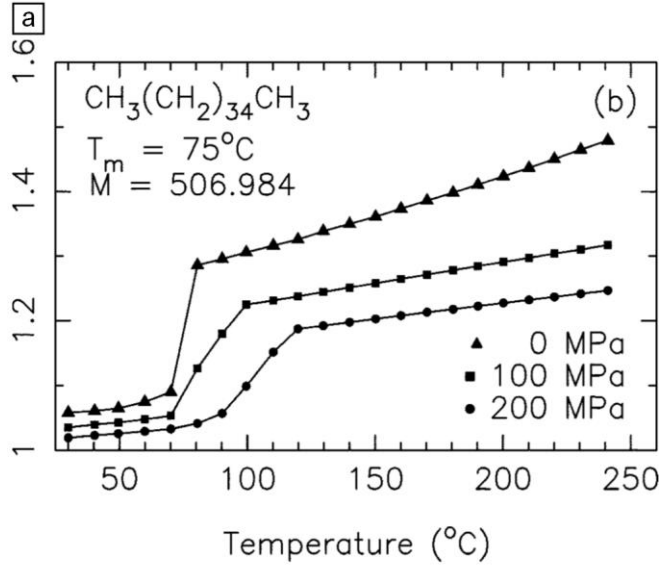


Figure 4. Demonstration of CNT-paraffin actuator as a passive thermal switch: (a) Simplified setup of measurement configuration; (b) measured heat flux through the actuator versus gap between the surfaces.



**b** ACTUATION ENERGY DENSITY FOR SEVERAL LOW VOLTAGE MICROACTUATORS

Actuation Type	$\mathcal{P}_a$ (J m <sup>-3</sup> )
Piezoelectric (PZT)	10 <sup>5</sup>
Electrostatic (comb-drive)	10 <sup>3</sup>
Electromagnetic	10 <sup>5</sup>
Thermal expansion (Ni/Si)	10 <sup>5</sup>
Thermo-pneumatic	10 <sup>6</sup>
Solid-liquid phase change (acetimide)	10 <sup>6</sup>
Shape memory Alloy (Ni-Ti)	10 <sup>7</sup>
<b>Solid-liquid phase † change (paraffin)</b>	<b>10<sup>7</sup></b>

Figure S1. Actuation characteristics of paraffin wax, from [3]. (a) Volume versus temperature of hexatriacontane (98%) under varying applied stresses, measured by high-pressure dilatometry. (b) Comparison of energy density for widely used active materials.

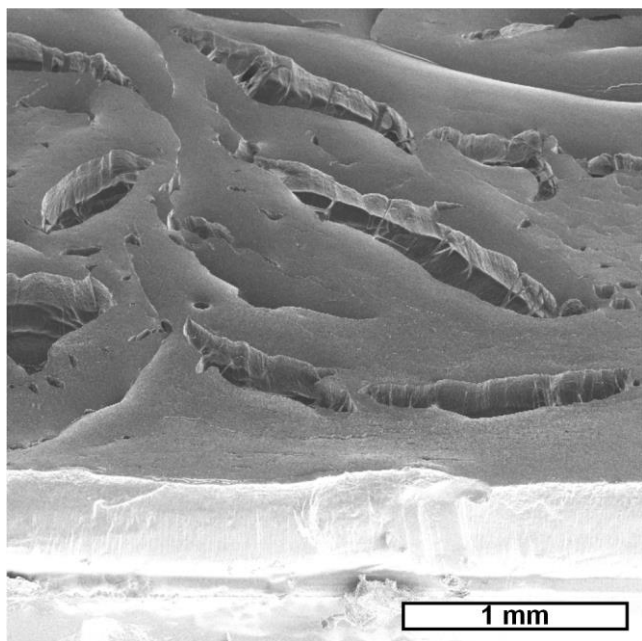


Figure S2. CNT-paraffin film that was infiltrated with paraffin then cooled without maintaining the applied compressive load. The SEM image shows large cracks that prevent vertical actuation of the film upon subsequent heating, because the segments of the composite instead expand laterally while the paraffin melts and expands.



Figure S3. Video (100X actual speed) showing the side view of a CNT-paraffin nanocomposite actuator upon three cycles from room temperature (approximately 20°C) to 175°C.

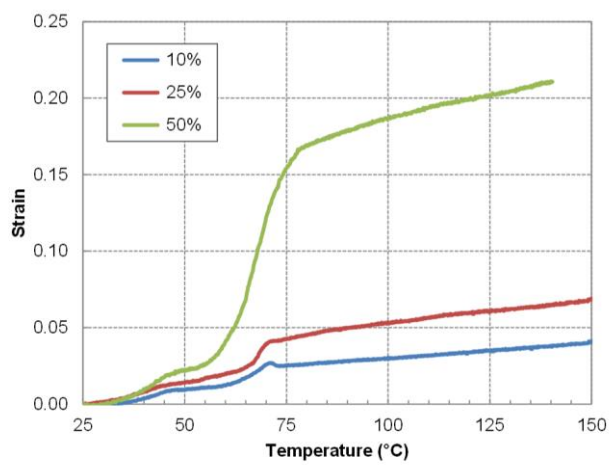


Figure S4. Strain-temperature curves of CNT-paraffin actuators that were fabricated under different amounts of compressive strain (relative to their initial height).

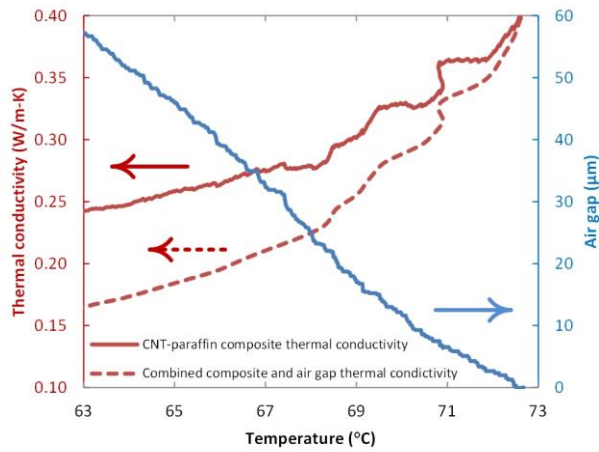


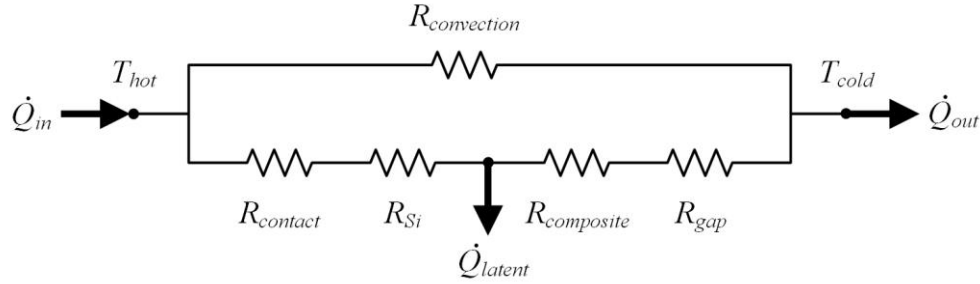
Figure S5. Characterization of self-activating CNT-paraffin thermal switch versus temperature: calculated composite thermal conductivity, combined thermal conductivity of composite and air gap thermal conductivity, and measured air gap.





## Appendix: Thermal resistance network model used to calculate CNT-paraffin thermal conductivity

The thermal conductivity of the CNT-paraffin composite was calculated from a thermal resistance network model, which is based on the experimental setup shown in Figure 4A and is drawn below.



In this model,  $\dot{Q}_{in}$  and  $\dot{Q}_{out}$  respectively denote the heat flux into and out of the system,  $\dot{Q}_{latent}$  is the heat absorbed by the composite to raise its temperature,  $T_{hot}$  and  $T_{cold}$  respectively denote the temperature of the heat source and the heat sink,  $R_{convection}$  denotes the convective thermal resistance of the air,  $R_{contact}$  denotes the contact resistance,  $R_{Si}$  denotes the resistance of the silicon substrate,  $R_{composite}$  denotes the resistance of the CNT-paraffin composite, and  $R_{gap}$  denotes the resistance of the air gap. Based on the model, the total thermal resistance is then calculated using

$$R_{total} = \left( \frac{1}{R_{convection}} + \frac{1}{R_{contact} + R_{Si} + R_{composite} + R_{gap}} \right)^{-1}. \quad (1)$$

Furthermore, the total thermal resistance can be calculated using the measured heat flux into the heat sink and the temperature difference between the heat source and the heat sink:

$$R_{total} = \frac{T_{hot} - T_{cold}}{\dot{Q}_{out}} \quad (2)$$

Combining Equations 1 and 2 allows us to solve for  $R_{composite}$ , since  $R_{convection}$  and  $R_{contact}$  have been independently measured and the values for  $R_{Si}$  and  $R_{gap}$  (corresponding to air thermal resistance) are known. Last, the thermal conductivity of the CNT-paraffin composite is calculated by taking the inverse of  $R_{composite}$ . This model assumes steady state conditions.

## Chapter 2: Replica molding of liquid crystal polymer microstructures for active surfaces

*Contents of this chapter is in preparation for publication as: H. Zhao, J.J. Wie, D. Copic, A.W. Orbaek, S. Kim and A.J. Hart, "Replica molding of liquid crystal polymer microstructures for active surfaces."*

### Introduction

Surfaces with dynamic micro- and nanoscale textures can potentially be used to manipulate friction drag, optical reflection, thermal transport, and other properties. However, in order to realize these applications, surfaces must be made consistently over large areas, and integrated with existing laminate and skin materials for use in vehicles such as aircraft.

Liquid crystal polymers are interesting candidate materials for active surfaces due to their tunable mechanical properties<sup>1-3</sup>, anisotropic expansion upon heating<sup>4</sup>, and opportunity for optically directed actuation<sup>5-7</sup>. For example, thin sheets made from stiff glassy liquid crystal network (LCN) polymers have been shown to oscillate at 30Hz with a tip displacement amplitude of 170°<sup>8</sup>. However, to our knowledge, miniaturization of LCN actuators in the form of surface-bound micropillars has not been demonstrated.

We present a replica molding (RM) fabrication technique<sup>9</sup> to obtain high fidelity surface bound glassy LCN microstructure actuators over large areas. The removal of oxygen during curing was critical to achieve high-fidelity replicas with smooth surface texture, while the necessary LCN alignment for actuation was obtained via curing in a magnetic field. Cast microstructures had lateral dimensions of a few microns and aspect ratios (AR) up to 15:1. A gradient based edge detection algorithm<sup>10</sup> was used to quantify the LCN microstructure actuation, verifying anisotropy of the network.

### Methods

LCN microstructure arrays were fabricated by replica molding within a magnetic field in a controlled atmosphere. The experimental setup includes a custom magnetic circuit designed to straighten and confine a magnetic through the sample. The magnetic yoke was placed inside a vacuum jar, whose aluminum base was in contact with a hotplate and is shown in Fig. 1a. A green LED light source, used for cross-linking, was located outside of the vacuum jar.

A LC powder mixture composed of 20 wt% optically active 4,40-bis[6-(acryloxy)hexyloxy] azobenzene monomers (A6Z6 from BEAM Co.), 78 wt % thermally active RMM491 monomer mixture (EMD Millipore), and 2 wt % I-784 photoinitiator (Ciba) was created<sup>1</sup>. The constituents of the RMM491 mixture and the optically active LC monomer, labeled A6Z6, are shown in Fig. 1b.

Master templates can be fabricated using standard silicon dry etching processes, or alternatively CNT/SU-8 composite microstructures may be used to fabricate complex 3D geometries<sup>9</sup>. From the master, a polydimethylsiloxane (PDMS) negative was cast and used to create the LCN replicas. PDMS was vacuum cast over the deep reactive ion etch (DRIE) patterned silicon master and cured at 120°C for 20min to form the negative mold (Fig. 1c). The powder mixture was added to the negative and heated to 110°C for 10 min at a pressure below 1 Torr (Fig. 1d). The magnetic field (0.3T) applied by the fixture causes benzene containing LC monomers to align in a cooperative fashion along it. The cooperative alignment of benzene rings inside a magnetic field was first suggested by de Gennes<sup>11</sup> and successfully demonstrated for use in liquid crystal polymers by Buguin et al.<sup>4</sup> The mixture was cooled to 75°C at 1°C/min resulting in a LC in the nematic phase with its director aligned along the magnetic field. Placing the sample in a strong magnetic field, which has been straightened via a magnetic yoke, and cooling it slowly achieves the necessary order and alignment for actuation. The sample was then exposed to green light (540 nm wavelength) for 40 min, which initiates cross-linking of the ordered LC monomers into a polymer network. After cooling to room temperature the LCN replica was manually demolded from the soft PDMS negative (Fig 1e).

A custom-built microscope was used to image the microstructures during actuation (Fig. 1f). This microscope has both a linearly polarized blue light and a white light source. During actuation the samples were exposed to linearly polarized blue light (~440 nm wavelength) aligned parallel to the LC director for 3-5 minutes. After actuation the sample was exposed to visible light for 15 minutes or heated to 90°C causing it to relax and recover its original shape. Azobenzene moieties predominantly take on the *trans* isomerization during the relaxation and the polymer network recovers its initial higher order nematic phase.

## Results and Discussion

We found that removal of oxygen was crucial for achieving high fidelity LCN replicas with low surface roughness. Samples cast without degassing have large voids due to air bubbles trapped in the molten powder mixture and have very large surface roughness (Fig. 2a). Fig. 2b shows a sample that was vacuum cast at 1 Torr to remove air bubbles from the molten powder mixture, after which air was reintroduced during curing. The bottom part of the SEM image shows the sample edge that was exposed to the air. Microstructures closer to the exposed edge have significantly larger surface roughness, suggesting that oxygen exposure impacts the crystallization of the LCN. We found that samples with large surface roughness have significantly reduced photogenerated strains.

Using these findings to drive process improvements, we show (Fig. 3) cast microstructures with a variety of sizes and shapes, with both small and large aspect ratios. Large microstructures with different cross-section shapes are shown in Fig. 3a, while large arrays of high aspect ratio (AR, height:width) structures are shown in Fig. 3b. The semi-cylindrical micropillars are 55  $\mu\text{m}$  tall and have an AR of approximately 15:1.

The LCN micropillars can be actuated by polarized blue light capable of providing sufficient energy to drive both the *trans-cis* and the *cis-trans* isomerization (Fig. 4a), due to an overlap between the *cis* and *trans* isomer absorption spectra<sup>12</sup>. The azobenzene *trans* isomer moieties absorb significantly less polarized light if they are oriented perpendicular the polarization, gradually creating a statistical buildup of such isomers. This buildup disturbs the nematic phase, reducing its order and achieving a volumetric shape change (Fig. 4b). This shape change can be used to alter either the height of a micropillar if the director is oriented along its axis (Fig. 4c) or the pillar cross section if the director is oriented perpendicular to it. Because the actuation is based on the disruption of the nematic LC phase, having good alignment prior to cross-linking the LC monomers is crucial. A comparison between similar LCN compositions and other actuating materials is shown in Fig. 4d<sup>13</sup>. Although the maximum generated stress of LCN materials are lower than that of other comparable polymers, we show that LCN materials can be cast into a verity of useful microstructures.

An interpolation-based edge tracking algorithm<sup>14</sup> was implemented to resolve sub-pixel actuation of cast LCN micropillars, imaged using the microscope described above. An SEM image and a top-down optical image of the optically active LCN microstructure are shown in Fig. 5a and 5b, respectively. We measured a photogenerated strain of 0.25% orthogonal to the

LCN director and a 0.11% contraction along it after 5 min of exposure to linearly polarized blue light oriented perpendicular to the LC director (Fig. 5c). The contraction along the director occurs because the rod-like stiff LC moieties gradually rotate away from it. Samples cured without the magnetic field showed no actuation. Previous studies with similar LCN compositions have measured a photogenerated strain along the director of 0.15% and a stiffness of 1.8 GPa using dynamic mechanical analysis (DMA)<sup>15</sup>. We expect that larger strains could be achieved via use of UV light, by achieving improved LCN alignment during the replica molding process, by composition reformulation at the expense of reduced stiffness<sup>1</sup>, and by physical aging of the material<sup>16</sup>.

## **Conclusion**

In conclusion, we have fabricated and tested LCN microactuators, exhibiting up to 0.25% strain along the director and a 0.11% contraction orthogonal to it after 5 min exposure of polarized blue light. For the first time, centimeter-scale areas of high aspect ratio microstructures were fabricated, enabled by careful environmental process control and removal of oxygen during casting. With further characterization and improvement of the optically-induced strain, this technology would be suitable for fabrication of active surface textures, such as for use in microfluidics, and possibly on the surfaces of miniature vehicles.

## **Acknowledgements**

Financial support was provided by the Air Force Office of Scientific Research (YIP Award FA9550-11-1-0089, program manager Dr. B.L. “Les” Lee). Microfabrication was performed at the Lurie Nanofabrication Facility (LNF), while electron microscopy was performed at the Michigan Electron Microbeam Analysis Laboratory (EMAL). We thank Dr. Timothy White (AFRL) for helpful insights, discussions, and provided materials. We also thank Ryan Oliver for contributions to the design and fabrication of the test apparatus.

## References

1. K. M. Lee, N. V. Tabiryan, T. J. Bunning, and T. J. White. Photomechanical mechanism and structure-property considerations in the generation of photomechanical work in glassy, azobenzene liquid crystal polymer networks. *J. Mater. Chem.* **2**, 691-698 (2012).
2. K. M. Lee, H. Koerner, R. A. Vaia, T. J. Bunning, and T. J. White. Relationship between the photomechanical response and the thermomechanical properties of azobenzene liquid crystalline polymer networks," *Macromolecules* **43**, 8185-8190 (2010).
3. A. Shimamura, A. Priimagi, J.-i. Mamiya, T. Ikeda, Y. Yu, C. J. Barrett, *et al.* Simultaneous analysis of optical and mechanical properties of cross-linked azobenzene-containing liquid-crystalline polymer films. *ACS Appl. Mater. Interfaces* **3**, 4190-4196 (2011).
4. A. Buguin, M. H. Li, P. Silberzan, B. Ladoux, and P. Keller. Micro-actuators: when artificial muscles made of nematic liquid crystal elastomers meet soft lithography. *J. Am. Chem. Soc.* **128**, 1088-1089 (2006).
5. Y. Yu, M. Nakano, and T. Ikeda. Photomechanics:directed bending of a polymer film by light. *Nature* **425**, 145-145 (2003).
6. C. L. van Oosten, C. W. M. Bastiaansen, and D. J. Broer. Printed artificial cilia from liquid-crystal network actuators modularly driven by light. *Nat. Mater.* **8**, 677-682 (2009).
7. M. Camacho-Lopez, H. Finkelmann, P. Palffy-Muhoray, and M. Shelley. Fast liquid-crystal elastomer swims into the dark. *Nat. Mater.* **3**, 307-310 (2004).
8. T. J. White, N. V. Tabiryan, S. V. Serak, U. A. Hrozhyk, V. P. Tondiglia, H. Koerner, *et al.* A high frequency photodriven polymer oscillator. *Soft Matter* **4**, 1796-1798 (2008).
9. D. Copic, S. J. Park, S. Tawfick, M. F. L. De Volder, and A. J. Hart. Fabrication of high-aspect-ratio polymer microstructures and hierarchical textures using carbon nanotube composite master molds. *Lab Chip* **11**, 1831-1837 (2011).
10. D. B. a. A. J. H. Assaf Ya'akovovitz and Davor Copic and Justin. Nanoscale displacement measurement of microdevices via interpolation-based edge tracking of optical images. *J. Micromech. Microeng.* **23**, (2013).
11. P.-G. d. Gennes and J. Prost, The physics of liquid crystals. Oxford : New York: Clarendon Press ; Oxford University Press (1993).
12. N. Tabiryan, S. Serak, X.-M. Dai, and T. Bunning. Polymer film with optically controlled form and actuation. *Opt. Express* **13**, 7442-7448 (2005).

13. S. Tawfick, M. De Volder, D. Copic, S. J. Park, C. R. Oliver, E. S. Polsen, *et al.* Engineering of micro-and nanostructured surfaces with anisotropic geometries and properties. *Adv. Mat.* **24**, 1628-1674 (2012).
14. A. C. Ya'akovovitz, D. Beroz, J. Hart, A. J. Nanoscale displacement measurement of micro-devices via interpolation-based edge tracking of optical images. *J. Micromech. Microeng.* **23**, 045004 (2013).
15. Y. Torres, T. White, A. McClung, and W. Oates. Photoresponsive azobenzene liquid crystal polymer networks: in situ photogenerated stress measurement. *ASME Conference Proceedings*, **2**, 39-45 (2010).
16. B. K. M. Lee, H. Koerner, D. H. Wang, L.-S. Tan, T. J. White, and R. A. Vaia. Tailoring the photomechanical response of glassy, azobenzene-functionalized polyimides by physical aging. *Macromolecules* **45**, 7527-7534 (2012).



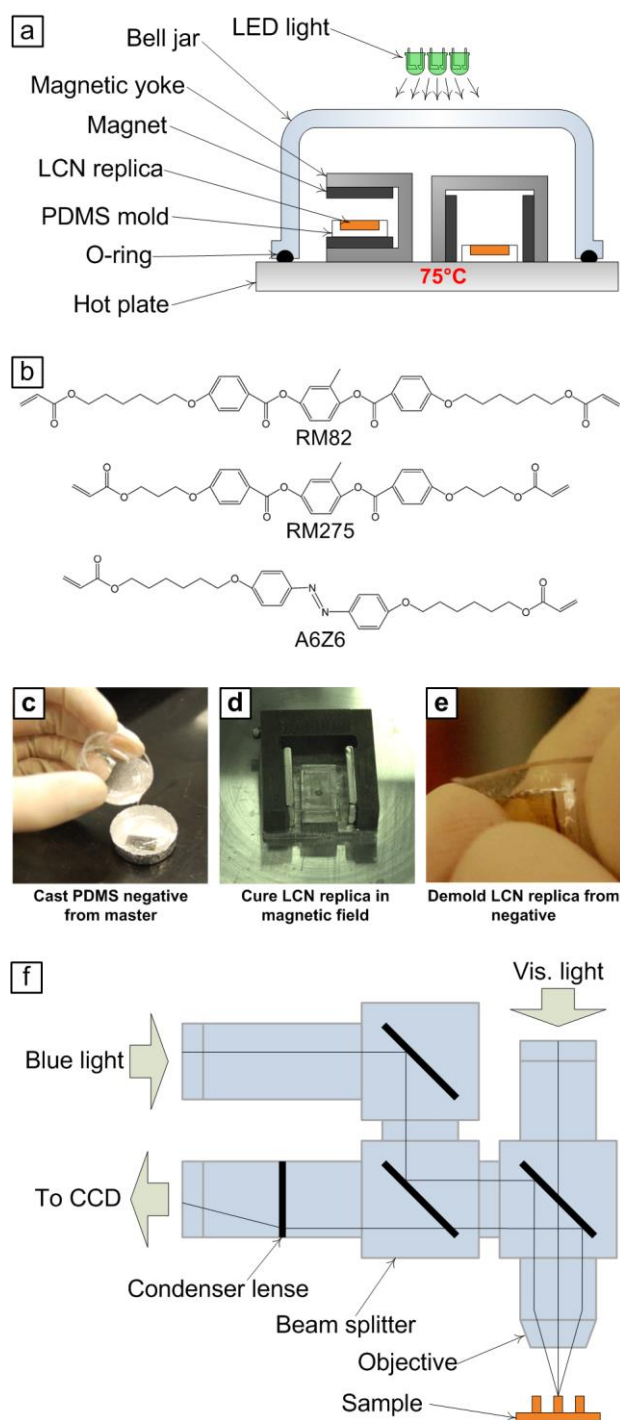


Fig. 1. (a) Experimental setup used to cast LCN micro-structures. (b) Casting of the PDMS negative from the DRIE etched silicon master. (c) Close up of molten LC mixture inside the magnetic field. (d) Manual demolding of replicated structures. (e) Diagrams of the monomers used in the LCN mixture. (f) Schematic of custom microscope schematic used during testing.

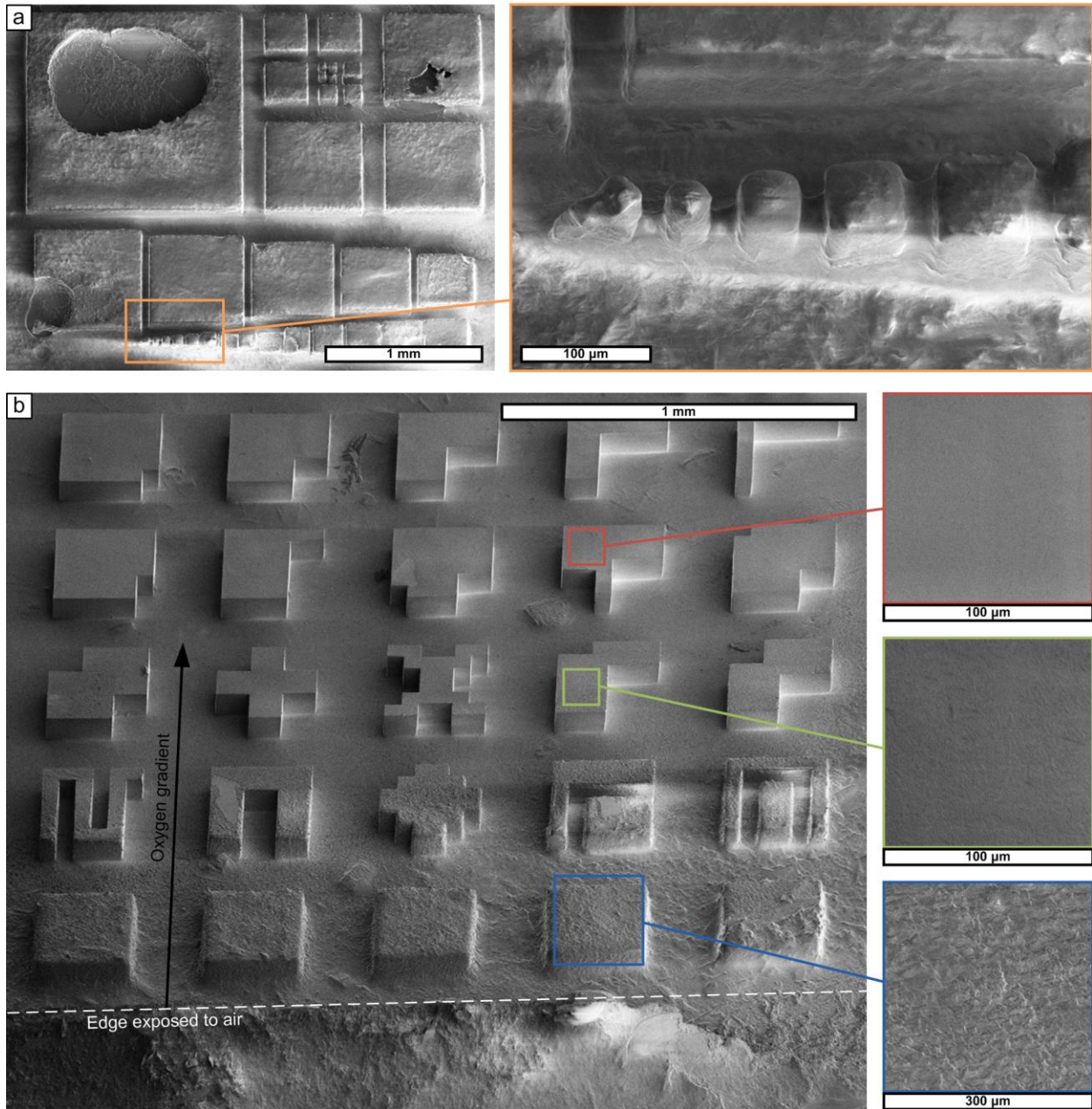


Figure 2. (a) LCN replicas cast without degassing of the molten LC mixture. (b) Degassed replica that was exposed to air during curing with close up images of selected regions, showing increased surface roughness in the presence of oxygen.

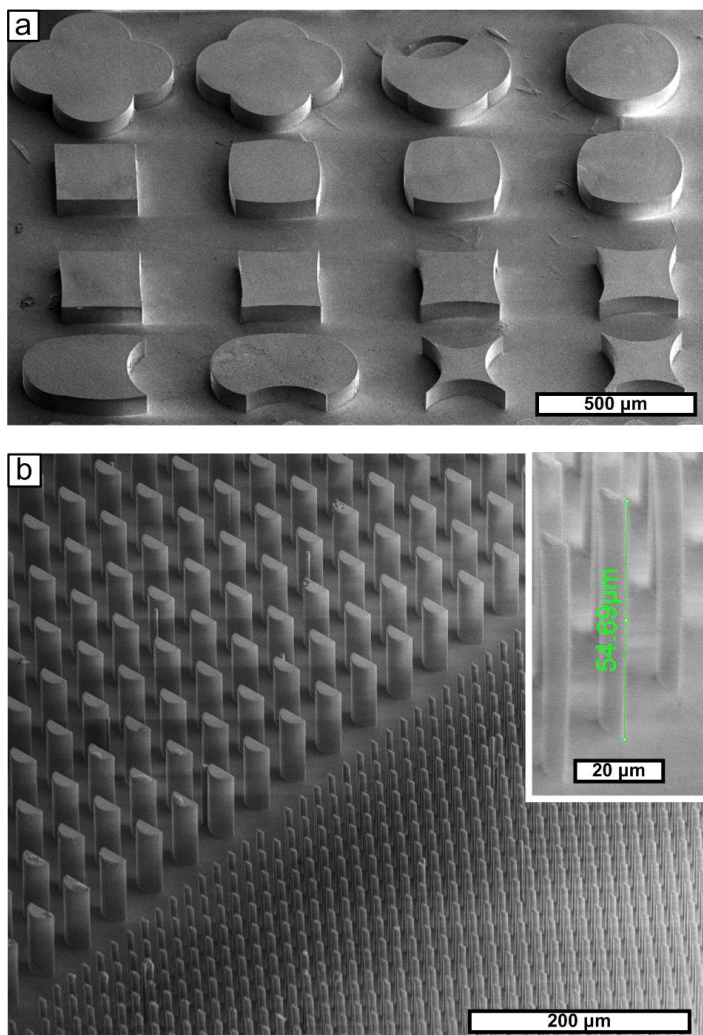


Figure 3. (a) Heterogeneous low aspect ratio optically active LCN microstructures. (b) High yield, large area array of asymmetric microstructures. Inset shows close up image of microstructures.

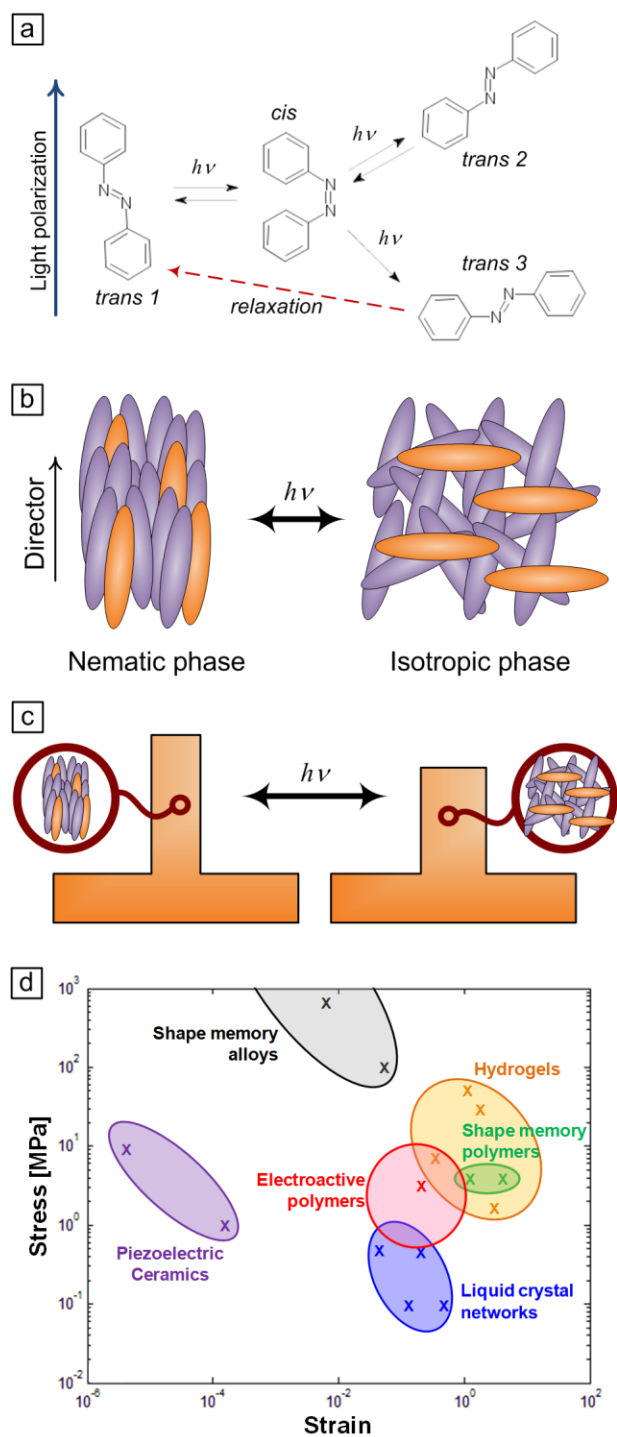


Figure 4. (a) *trans-cis-trans* isomerization of azobenzene due to polarized blue light exposure. (b) Schematic of nematic and isotropic LCN phase containing thermally active (purple) and optically active LC molecules (orange). (c) Volumetric shape change due to LCN phase change. (d) Maximum stress and strain generated by comparable actuating materials <sup>13</sup>.

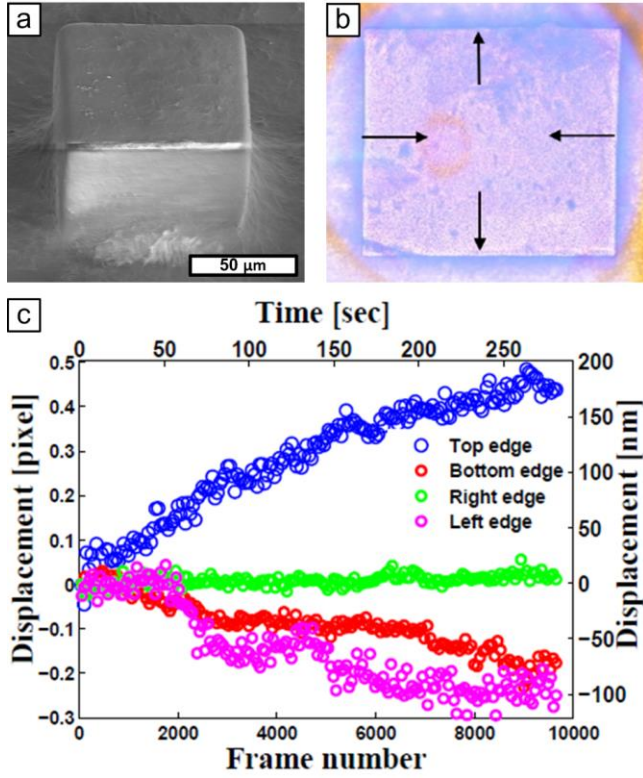


Figure 5. (a) SEM image of optically active LCN micropillar. (b) Sample optical image of the top-down view from a custom microscope used in for edge tracking. Arrows indicate strain direction. (c) Results of gradient based edge tracking algorithm, showing edge movement.



### Chapter 3: Strain-engineered manufacturing of freeform carbon nanotube microstructures

*Contents of this chapter have been published as: M.De Volder, S. Park, S. Tawfick and A.J. Hart, "Strain-engineered manufacturing of freeform carbon nanotube microstructures." Nat. Commun. 5, 4512 (2014).*

#### Introduction

Scalable fabrication of microstructures that mimic the hierarchical surface designs found in nature has been a long-standing aspiration of material scientists<sup>1-5</sup>. While symbiotic growth of the integrated circuit (IC) and micro electro mechanical systems (MEMS) industries has enabled innovations in 3D fabrication that leverage semiconductor processing tools, these methods, such as interference or inclined exposure lithography are typically limited to arrays of identical structures<sup>6-8</sup>. Rapid prototyping methods such as direct laser writing, multiphoton lithography, and focused ion beam milling can create arbitrary forms but are serial, and therefore have lower areal throughput<sup>9,10</sup>. It is also especially difficult to fabricate surface structures having curved and/or re-entrant geometries.

On the other hand, use of locally directed actions, such as mechanical stresses, capillary forces, and electromagnetic fields, along with their interactions with templates, offers opportunity to create novel self-organized geometries and to design fabrication processes that achieve attractive combinations of dimensional control and throughput<sup>2,8,11-15</sup>. Examples abound in soft materials and chemical systems including micro-scale reaction-diffusion patterns<sup>16,17</sup>, self-assembly of block copolymers<sup>18</sup>, and helical aggregation of polymer nanopillars<sup>19,20</sup>. However, many of these processes need further development to achieve structural uniformity over large substrates.

We present a novel approach taking advantage of microscale top-down lithographic patterning in conjunction with nanoscale self-organization, which enables large-area fabrication of freeform microstructures made of aligned carbon nanotubes (CNTs). This process leverages the influence of the catalyst-substrate interactions on the growth rate of CNTs<sup>21</sup>, creating stress gradients during synthesis that guide the CNTs into curved microscale geometries. Our method is analogous to the well-known use of thin film stress to create curved and folded MEMS structures<sup>22</sup>. However, because our process is based on an additive chemical synthesis process instead of a subtractive etching and release technique, it enables the direct synthesis of complex

microstructures that are perpendicular rather than parallel to the substrate. This has two major implications: it enables fabrication of closely packed arrays of structures with heterogeneous shapes, and the porosity of the CNT forests enables conformal coating after growth to modify chemical and/or mechanical properties. We demonstrate this latter point by conformal coating of CNT “microtruss” arrays by atomic layer deposition (ALD) and polymer CVD, which increases their mechanical stiffness without changing the geometry.

## Methods

*Substrate patterning and CNT growth:* The catalyst and TiN layers are patterned on (100) silicon wafers with 300 nm of thermally grown SiO<sub>2</sub>. Each layer is patterned by lift-off processing, by photolithography (photoresist IX845) followed by ultrasonic agitation in acetone. The TiN layer is deposited and patterned first, and then the catalyst layer (1 nm Fe upon 10 nm Al<sub>2</sub>O<sub>3</sub>) is deposited and patterned. The wafer is then diced into ~1×1 cm pieces, and the substrates are placed in the quartz tube furnace, and the CNT growth is performed. The recipe starts by with flowing 100/400 sccm of He/H<sub>2</sub> while heating to 775 °C over 10 minutes (ramping step); then the system is held at 775 °C for 10 minutes (annealing step) while maintaining the gas flow. Then 100 sccm of C<sub>2</sub>H<sub>4</sub> is added to the gas mixture at 775 °C for CNT growth for the desired duration. The typical growth rate is ~50 μm/minute on Fe/Al<sub>2</sub>O<sub>3</sub>/SiO<sub>2</sub>. Once the CNTs have grown, C<sub>2</sub>H<sub>4</sub> is removed from the gas mixture and the furnace is cooled to <100 °C. After cooling, the system is purged with He before the sample is removed. Optionally, C<sub>2</sub>H<sub>4</sub> flow can be maintained while cooling down to improve the adhesion of the CNT microstructures to the substrate. Once the cooling step is complete, the quartz tube is purged with 1000 sccm of He for 5 minutes before opening up the end caps and retrieving the samples.

*Small Angle X-ray Scattering (SAXS):* SAXS characterization of CNT microstructures was performed at the Cornell High Energy Synchrotron Source (CHESS) using the G1 beamline (10±0.1 keV, 0.13nm wavelength). The beam is focused to a 10μm spot using a single bounce monocapillary. The CNT sample is placed on a motorized stage and the focused X-ray beam is passed through the sample. The scattered beam is collected using a 2D detector and the measured intensities were normalized to the original intensity measured by another detector at upstream of the CNT sample. The scattering data is then fitted to a mathematical model assuming a log-

normal distribution of hollow cylinders to calculate the CNT diameters as well as the Herman's parameter for CNT alignment. The detailed procedure is described by Bedewy et al.<sup>30</sup>.

## Results and Discussion

**Fabrication.** CNTs grown by chemical vapour deposition (CVD) from a high-density arrangement of catalyst nanoparticles on a substrate are known to self-organize into vertically aligned assemblies often called “CNT forests”<sup>23,24</sup>. We first observed that the density and rate of CNT forest growth from a widely studied supported catalyst (Fe/Al<sub>2</sub>O<sub>3</sub>, 1/10 nm) can be influenced by the material immediately beneath the catalyst. This premise is shown in Fig. 1a; patterning of CNT growth catalyst (Fe/Al<sub>2</sub>O<sub>3</sub>) on a SiO<sub>2</sub>/TiN “checkerboard” followed by exposure to standard CVD conditions (see Methods) results in a “bi-level” CNT micropillar array. The catalyst patterns directly on SiO<sub>2</sub> grow CNTs to ~100  $\mu$ m (in < 2 minutes), whereas the patterns on TiN (upon SiO<sub>2</sub>) grow CNTs to 50  $\mu$ m in the same time span. In Fig. 1b, “tri-level” CNT forests are grown by arranging patches of catalyst on SiO<sub>2</sub>, 70 nm TiN, and 140 nm TiN. This principle could be extended to an arbitrary number of levels or even continuous height gradients via additional lithography and underlayer deposition steps that modulate the growth rate via catalyst-substrate interactions.

Next, we used the above differential growth principle to design compound catalyst/underlayer patterns that directly form curved CNT forest geometries. If a continuous micro-scale catalyst pattern is placed partially on SiO<sub>2</sub> and partially on TiN, the differential growth rates induce stress within the CNT microstructure. For example, as shown in Fig. 2a and 2b, a square catalyst pattern with half of its area on the TiN layer bends toward the side which is upon TiN, due to the difference in growth rate on the coupled halves of the structure. The stress is transferred between contacting CNTs at the boundary region via mechanical entanglement and van der Waals interactions among the CNTs. Depending on the curvature and length of the structures, slanted micropillars (Fig. 2a), or arches (Fig. 2b) can be fabricated. Because the local interaction and differential growth rate determines the trajectory of each structure, large arrays with nearly identical anisotropic shapes can be produced as shown in the SEM images. Importantly, these 3D structures are fabricated using only two standard photolithography steps, one for patterning the TiN layer, and one for patterning the catalyst layer.



The curvature can be controlled by designing the amount of overlap between the catalyst and the TiN underlayer. This is illustrated in Fig. 3a and b, which respectively show arrays of round and square cross-section micropillars where the overlap distance is varied from left to right (increments of 5  $\mu\text{m}$ ). As expected, the portion of the pillars growing on TiN is always shorter, and as a result, all pillars bend towards the TiN side. As the portion of overlap decreases, the stress induced by the differential growth rate causes increased bending (smaller radius of curvature), reaching a maximum when the catalyst shape is split symmetrically by the TiN layer. With <50% overlap on TiN, the curvature increases gradually until the structure is only slightly curved at the rightmost extent of the array. The CNTs are generally tangential to the curvature of the microstructures, similar to the CNT alignment observed in CNT forests.

**Static model of stress-driven CNT curvature.** The coupling of stress and CNT growth rate, via the anisotropic mechanics of the CNT forest<sup>25</sup>, is a complex problem. However, we find that a static mechanical model analogous to that used for differential expansion of a bi-material cantilever beam can reasonably predict the curvature of CNT structures grown from an overlapped catalyst/TiN rectangle. Starting from the classical formulation of the bimetallic strip model<sup>26</sup>, we replace the temperature-dependent expansion term by a differential lengthening term representing the CNT growth rate. Accordingly, the curvature of the compound CNT microstructure is described as:

$$\frac{1}{\rho} = \frac{6\left(\frac{R_1 - R_2}{R_1}\right)(1+m)^2}{w\left(3(1+m)^2 + (1+mn)\left(m^2 + \frac{1}{mn}\right)\right)} \quad (1)$$

Here  $\rho$  is the radius of curvature,  $R_1$  and  $R_2$  are the growth rates (1 denotes CNTs on Fe/Al<sub>2</sub>O<sub>3</sub>/SiO<sub>2</sub> and 2 denotes CNTs on Fe//Al<sub>2</sub>O<sub>3</sub>/TiN), and  $w$  is the CNT micropillar width. In addition,  $m$  and  $n$  are defined as

$$m = \frac{w_2}{w_1}, n = \frac{E_2}{E_1} \quad (2)$$

where  $w$  denotes the width and  $E$  denotes the respective Young's Moduli of the segments. The value of  $n$  is specified as 0.6 which is the ratio of the measured areal mass density of CNTs on the respective underlayers; however, because the elongation of each layer is specified in the model, the output is insensitive to this value. The geometric parameters are defined in Fig. 3c.

Using the calculated curvatures, and the weighted average growth rate, the shapes of the resultant CNT microstructures were visualized using Matlab. The simulation results correspond to the rows of structures in the SEM image Fig. 3b. To compare the experiments to the

simulation, the tip position was characterized in horizontal and vertical axes, normalized to the base dimension ( $w$ ), as shown in Fig. 3c. For both the experiment and simulation, the  $x$  position of the tip reaches its maximum at 0.4 overlap, and the  $y$  position reaches its minimum at approximately 0.6-0.7 overlap.

The differences between the predicted and calculated displacements arise because the model does not capture the exact kinetics of CNT growth, which varies with time. Moreover, it cannot consider how the stress between the two portions of the structure, which are idealized as perfectly coupled without slip, influences the deformation. CNT forests have anisotropic mechanical properties, with the lateral stiffness (perpendicular to the CNT alignment) typically much less than the axial stiffness<sup>27</sup>, therefore in principle favoring greater deflection due to built-in stress gradient. Local wrinkling and buckling of the CNTs in the compound microstructures indicates that the growth stress causes complex mechanical deformations, which cannot be predicted by linear elasticity and the bimaterial deflection model (see Fig. 4a).

To gain further insight into the mechanical coupling causing stress-driven bending, we designed a “striped” structure where alternate catalyst/underlayer regions are coupled with a large interfacial area. This structure is symmetric, so it grows straight vertically yet has significant internal stresses. As shown in Fig. 4a and the neighboring insets, the faster growing CNTs deform collectively into a wavelike pattern. Therefore, while the vertical growth rate of the structure is matched at the interface, the faster growing side still accumulates longer CNTs and these CNTs bend and possibly buckle to accommodate their additional length. This deformation mode is similar to what is observed in mechanically compressed forests<sup>28</sup>.

As seen in Fig. 3a and supplementary figure 1a, some structures separate at the interface between the differentially growing regions, due to shear stresses at the interface. In future work, this could be remedied by adapting the structure design to reduce the interfacial shear stress between the segments, or by using a more gradual growth rate gradient to accommodate the stress gradient, such as a three-layer design as in Fig. 1b. However, we importantly find that structures that do not separate during synthesis can withstand large subsequent deformations without failure. For instance, supplementary figure 1b shows an SEM image of an arrangement of bent pillars during compression to 50% vertical strain, at which point delamination at the interface begins only where the pillars kink near their midsection.

**CNT and catalyst morphology.** The strain-engineered CNT microstructures show differing CNT density and alignment in the fast and slow growing portions. In Fig. 4a,b, the CNTs grown from catalyst on TiN appear to have greater vertical alignment influenced by the interface with the faster-growing region. On the other hand, the CNTs grown from catalyst on SiO<sub>2</sub> are less aligned, due to the retarding force from the slower-growing mating regions.

We hypothesized that the differential CNT growth behavior on the TiN underlayer may be attributed to differences in the catalyst morphology, which can influence the CNT diameter distribution and number density. Atomic Force Microscopy (AFM) showed that as-deposited catalyst layers on SiO<sub>2</sub> and TiN have a similar topology (supplementary figure 2). However, upon annealing in H<sub>2</sub>/He prior to hydrocarbon exposure (see methods), the TiN-catalyst layer forms shallow mounds, tens of nanometers high and hundreds of nanometers wide, in addition to smaller catalyst particles. The control case of catalyst on SiO<sub>2</sub> does not exhibit such topography. For samples with 80 nm TiN layer, the average catalyst particle height and spacing were calculated to be 5.2 nm and 19 nm respectively. Compared to those on SiO<sub>2</sub> (7.5 nm and 18 nm, respectively <sup>29</sup>), the catalyst particle sizes are smaller on average while the spacing is comparable. In addition, the Root Mean Square (RMS) roughness of the annealed catalyst/TiN layer is 5.6 nm, which is considerably higher than that of catalyst on SiO<sub>2</sub> (1.4 nm).

Small Angle X-ray Scattering (SAXS) was used to further investigate the CNT forest morphology <sup>30,31</sup>. For this experiment, CNTs were grown for 10 minutes on SiO<sub>2</sub>, and on 40 nm, and 80 nm TiN layers; these samples reached lengths of 800, 500, and 400  $\mu$ m respectively. The scattered X-ray intensities were fitted to a mathematical form factor model for hollow cylinders <sup>32</sup> to calculate the diameter and Herman's orientation parameter, which is a measure of alignment. Both the CNT diameter (Fig. 4e) and alignment (supplementary figure 3) are shown to be lesser for increasing TiN underlayer thickness. Specifically, CNTs on SiO<sub>2</sub> have initial average diameter of 9.5 nm, while CNTs on TiN are approximately 8 nm in diameter. These measurements further support the AFM data which showed that the catalyst particles on TiN layers are smaller than those on SiO<sub>2</sub>. The decrease in diameter with growth time has been attributed to diffusion of the catalyst into the Al<sub>2</sub>O<sub>3</sub> <sup>30,33</sup>. The Herman's orientation parameter increases from the top of the forest (the initial growth), then reaches a maximum, and then decreases toward the bottom of the forest. This trend is typically observed for CNT forests grown by CVD, and has been attributed to density variation due to collective activation and

deactivation of the growing CNT population<sup>30</sup>. The measured areal mass density of the CNT forests is 0.011 mg mm<sup>-2</sup> on 80 nm TiN and 0.018 mg mm<sup>-2</sup> on SiO<sub>2</sub>. Therefore, these methods consistency show that placement of the TiN layer under the catalyst results in CNT forests with a smaller average CNT diameter, lesser alignment of CNTs, and a lower density. Although we have not directly compared the mechanical properties of the different segments, we expect that the CNT forests on TiN have lower stiffness, and lesser anisotropy in mechanical properties. The positive correlation between CNT density and alignment is also expected based on recent literature, which demonstrated that CNT-CNT crowding controls alignment within non-patterned forests<sup>34</sup>.

Based on our understanding of the elementary catalyst/underlayer designs that achieve unidirectional bending, we designed a variety of more complex patterns that produce exemplary CNT microstructures having complex curvature. For instance, a compound shape consisting of a “+” catalyst microfeature with each arm offset by a rectangular TiN underlayer results in growth of twisted CNT microstructures (Fig. 5a), resembling macroscale propellers. The first-order applicability of the bimaterial bending model discussed above inspired us to evaluate the suitability of finite element modeling (FEM) to predict the shapes of these structures. These were simulated using Comsol FEM software as illustrated in Fig. 5a, capturing the uncoupled differential growth rate (Fig. 1a) as a 50% expansion mismatch, and estimating the Young’s modulus as 30 MPa for the CNTs on TiN and 50 MPa on SiO<sub>2</sub><sup>35</sup>.

Similarly, thin semicircles of CNTs can be directed to curve outward by offsetting the TiN underlayer as shown in Fig. 5b. Further structural complexity is shown by the scrolling of thin offset rectangular patterns (Fig. 5c). Last, exotic hierarchical arrangements can be formed by the interaction of closely spaced structures, such as the self-organization of offset circular micropillars into wavy patterns (Fig. 5d) that are reminiscent of macroscale crochet stitching. We hypothesize that, after the individual structures bend unidirectionally and contact one another, their continued growth and steric hindrance causes the wavy pattern to form. More investigation is needed to understand the complex deformations of these structures, and their relationship to the mechanics of the CNT forest and the mechanical feedback on the growth process itself.

Notably, in spite of the complex geometries and local deformations, all of these structures can be produced with impressive consistency over large arrays. Arrays of several hundred

structures were examined and shown to exhibit nearly identical forms, with defects most frequently arising from debris due to the lithography process rather than the CNT growth step. In this study, we explored structures with critical dimensions as small as 5  $\mu\text{m}$  (Fig. 5), and found that the uniformity of the structures was not sacrificed at this scale. We expect that smaller 3D microstructures could be made while still using optical lithography along with high-precision alignment of the catalyst and TiN layers. Notably, sub-micron vertical CNT features have been fabricated for use as interconnects<sup>36</sup>. Further, because the curved and twisted geometries result from collective behavior of CNT forest growth, we expect the structures to require a certain minimal size to average out the stochastic variation of individual CNT growth rate and catalyst lifetime. Considering the approximate CNT-CNT spacing within the current microstructures ( $\sim 100$  nm), the minimal feature size of reliable growth of curved microstructures may be limited to  $\sim 1$   $\mu\text{m}$ , though this requires further investigation.

Last, we show that 3D CNT structures can be post-processed via both wet and dry methods that enable tuning of their properties and functionality. Low-density bent CNT micropillars can be transformed into robust densely packed CNT structures by capillary forming (Fig. 6a-b)<sup>35,37,38</sup>. To do so, the substrate is exposed to a stream of heated acetone vapor, causing acetone to condense onto the CNTs and substrate, and infiltrate each CNT microstructure. Upon subsequent evaporation of the acetone, the CNT forest shrinks laterally, due to the surface tension of the shrinking meniscus. Previously, we showed that capillary forming of vertical CNT microstructures increases the Young's modulus in compression approximately 100-fold, from  $\sim 50$  MPa to 4 GPa<sup>35</sup>. These values are comparable to soft rubbers and stiff epoxies, respectively. Moreover in the present case the capillary forming process preserves the curved geometry and increases the lateral deflection.

Alternatively, curved CNT microstructures can be coated conformally via vapor phase methods, thereby enabling decoupled control of geometry and mechanical properties. To investigate this, we fabricated CNT "microtruss arrays" (Fig. 6c-e), which are analogous to truss designs used in composite materials to achieve high strength and energy absorption at relatively low density<sup>39-41</sup>. The CNT microtrusses each consist of four corner members and a central pillar, meeting at an apex. We explored coating of the CNT microtrusses with both parylene (by chemical vapor deposition, CVD, supplementary figure 4) and alumina (by atomic layer deposition, ALD, Fig. 6d). Upon vapor phase infiltration of the precursors, the CNTs and

bundles within the forest are coated individually and conformally <sup>42</sup>, enabling fine-tuning of their porosity and mechanics without altering the microstructure geometry. Via flat punch compression testing, we found that a 51 nm Al<sub>2</sub>O<sub>3</sub> coating on the CNTs increases the mechanical stiffness by more than 100-fold; typical loading-unloading curves are shown in Fig. 6e and supplementary figure 4 for different coating materials and thicknesses. The equivalent stiffness range of the 3D CNT microtrusses is 0.36 to 54 kN m<sup>-1</sup>, which spans typical values of MEMS springs used in probe card arrays <sup>43</sup>. A further attribute of the TiN underlayer is its electrical conductivity. In the future, electrical integration of strain-engineered CNT structures in conjunction with the post-processing methods described above could be useful in advanced microsystems, including as structural elements or microsensors <sup>44,45</sup>. Such applications could take advantage of the thermal and mechanical durability of CNTs, as well as the anisotropic properties arising from their alignment and collective curvature.

The ability to fabricate large arrays of 3D microstructures is also conducive to mimicry of nature's advanced functional materials <sup>5</sup>. We say this because the structures shown in Fig. 2 and 5 have similar size and geometry to butterfly wings that have anisotropic wetting properties <sup>46</sup>, dry adhesive contacts on the legs of beetles and gecko lizards <sup>3</sup>, and microscale sensing hairs found on spiders <sup>47</sup>. Therefore, we suggest that 3D CNT microstructures offer opportunities to further engineer the excellent dry adhesive <sup>48,49</sup> and superhydrophobic <sup>50</sup> properties previously reported for CNT forests. For mechanical applications such as dry adhesion, an important consideration is the adhesion of the structures to the substrate, as well as the mechanical resilience of the structures upon repeated loading. While we have found that the segments of the curved structures are well adhered to each other (supplementary figure 1b), we anticipate that coating or transfer steps may be necessary to anchor the structures for use as robust surface contacts <sup>49</sup>. Exploration of potential optical and photonic applications would require further miniaturization of the structures. Nevertheless, combined with the emerging methods to grow and pattern CNT forests on large-area substrates <sup>51-53</sup>, we are optimistic that the methods shown here can enable large-area surface coatings having advanced functionalities.

## Conclusion

In summary, we show that strain-engineered CNT growth enables the scalable fabrication of complex 3D microstructures having unidirectional and multidirectional curvature. The

capability to produce such structures *en masse* using only 2D patterning methods along with standard thermal processing contrasts the limitations of many existing processes that require serial processing or sequential exposure using complex inclined lithography methods. Moreover, the structures can profit from the mechanical robustness and electrical conductivity of CNTs, and their mechanical and surface properties can be engineered independently from their geometry by conformal coating of the CNTs after growth. This represents a highly attractive principle for materials design, and is promising for scalable manufacturing of 3D microstructured surfaces having biomimetic properties.

### **Acknowledgements**

Financial support to M.D.V was provided by the European Research Council (ERC - HIENA), and the fund for scientific research FWO. Financial support to S.J.P., S.T., and A.J.H. was provided by the Defense Advanced Research Projects Agency (HR0011-10-C-0192) and the Air Force Office of Scientific Research (Young Investigator Program, 11-NA-018). Support from DARPA was received under Agreement to NextGen Aeronautics, and any opinions, findings, and conclusions or recommendations expressed in this material do not necessarily reflect the views of NextGen Aeronautics and/or DARPA. Microfabrication was performed at imec and the Lurie Nanofabrication Facility (LNF), which is a member of the National Nanotechnology Infrastructure Network (NNIN); and electron microscopy was performed at imec and the Michigan Electron Microbeam Analysis Laboratory (EMAL). SAXS measurement was performed at Cornell High Energy Synchrotron Source (CHESS). We thank Mostafa Bedewy for assistance with X-ray scattering measurements and data analysis.

## References

1. Aizenberg, J. et al. Skeleton of *Euplectella* sp.: Structural hierarchy from the nanoscale to the macroscale. *Science* **309**, 1112255 (2005).
2. Grinthal, A. et al. Steering nanofibers: An integrative approach to bio-inspired fiber fabrication and assembly. *Nano Today* **7**, 35-52 (2012).
3. Arzt, E., Gorb, S. & Spolenak, R. From micro to nano contacts in biological attachment devices. *Proc. Natl. Acad. Sci. U.S.A.* **100**, 10603-10606 (2003).
4. Fratzl, P. & Weinkamer, R. Nature's hierarchical materials. *Prog. Mater. Sci.* **52**, 1263-1334 (2007).
5. Bae, W.-G. et al. 25th anniversary article: scalable multiscale patterned structures inspired by nature: the role of hierarchy. *Adv. Mat.* **26**, 675-700 (2014).
6. Campbell, M., Sharp, D. N., Harrison, M. T., Denning, R. G. & Turberfield, A. J. Fabrication of photonic crystals for the visible spectrum by holographic lithography. *Nature* **404**, 53-56 (2000).
7. Del Campo, A. & Greiner, C. SU-8: a photoresist for high-aspect-ratio and 3D submicron lithography. *J. Micromech. Microeng.* **17**, R81-R95 (2007).
8. Tawfick, S. et al. Engineering of micro- and nanostructured surfaces with anisotropic geometries and properties. *Adv. Mat.* **24**, 1628-1674 (2012).
9. Bertsch, A., Jiguet, S. & Renaud, P. Microfabrication of ceramic components by microstereolithography. *J. Micromech. Microeng.* **14**, 197-203 (2004).
10. Stampfl, J. et al. Photopolymers with tunable mechanical properties processed by laser-based high-resolution stereolithography. *J. Micromech. Microeng.* **18**, 0960-1317 (2008).
11. Whitesides, G. M. & Grzybowski, B. Self-assembly at all scales. *Science* **295**, 2418-2421 (2002).
12. Grzelczak, M., Vermant, J., Furst, E. M. & Liz-Marzán, L. M. Directed self-assembly of nanoparticles. *ACS Nano* **4**, 3591-3605 (2010).
13. De Volder, M. & Hart, A. J. Engineering hierarchical nanostructures by elastocapillary self-assembly. *Angew. Chem. Int. Ed.* **52**, 2412-2425 (2013).
14. Futaba, D. N. et al. Dual porosity single-walled carbon nanotube material. *Nano Lett.* **9**, 3302-3307 (2009).



15. De Volder, M. F. L., Tawfick, S., Park, S. J. & Hart, A. J. Corrugated carbon nanotube microstructures with geometrically tunable compliance. *ACS Nano* **5**, 7310-7317 (2011).
16. Grzybowski, B. A., Bishop, K. J. M., Campbell, C. J., Fialkowski, M. & Smoukov, S. K. Micro-and nanotechnology via reaction-diffusion. *Soft Matter* **1**, 114-128 (2005).
17. Noorduyn, W. L., Grinthal, A., Mahadevan, L. & Aizenberg, J. Rationally designed complex, hierarchical microarchitectures. *Science* **340**, 832-837 (2013).
18. Scherer, M. R. J. & Steiner, U. Efficient Electrochromic devices made from 3D nanotubular gyroid networks. *Nano Lett.* **13**, 3005-3010 (2013).
19. Pokroy, B., Kang, S. H., Mahadevan, L. & Aizenberg, J. Self-organization of a mesoscale Bristle into ordered, hierarchical helical assemblies. *Science* **323**, 237-240 (2009).
20. Kang, S. H., Wu, N., Grinthal, A. & Aizenberg, J. meniscus lithography: evaporation-induced self-organization of pillar arrays into moire patterns. *Phys. Rev. Lett.* **107**, 177802 (2011).
21. Sam, E. D. et al. Simultaneous growth of self-patterned carbon nanotube forests with dual height scales. *Nanoscale* **4**, 3746-3753 (2012).
22. Chalapat, K. et al. Self-organized origami structures via ion-induced plastic strain. *Adv. Mat.* **25**, 91-95 (2013).
23. De Volder, M. F. L., Vidaud, D. O., Meshot, E. R., Tawfick, S. & Hart, A. J. Self-similar organization of arrays of individual carbon nanotubes and carbon nanotube micropillars. *Microelectron. Eng.* **87**, 1233-1238 (2010).
24. Hata, K. et al. Water-assisted highly efficient synthesis of impurity-free single-walled carbon nanotubes. *Science* **306**, 1362-1364 (2004).
25. Maschmann, M. R., Ehlert, G. J., Tawfick, S., Hart, A. J. & Baur, J. W. Continuum analysis of carbon nanotube array buckling enabled by anisotropic elastic measurements and modeling. *Carbon* **66**, 377-386 (2014).
26. Timoshenko, S. ANALYSIS OF BI-METAL THERMOSTATS. *J. Opt. Soc. Am.* **11**, 233-255 (1925).
27. Maschmann, M. R., Ehlert, G. J., Tawfick, S., Hart, A. J. & Baur, J. W. Continuum analysis of carbon nanotube array buckling enabled by anisotropic elastic measurements and modeling. *Carbon* **66**, 377-386 (2014).

28. Cao, A. Y., Dickrell, P. L., Sawyer, W. G., Ghasemi-Nejhad, M. N. & Ajayan, P. M. Super-compressible foamlike carbon nanotube films. *Science* **310**, 1307-1310 (2005).
29. Meshot, E. R. et al. High-Speed in Situ X-ray Scattering of Carbon Nanotube Film Nucleation and Self-Organization. *ACS Nano* **6**, 5091-5101 (2012).
30. Bedewy, M., Meshot, E. R., Reinker, M. J. & Hart, A. J. Population growth dynamics of carbon nanotubes. *ACS Nano* **5**, 8974-8989 (2011).
31. Wang, B. N., Bennett, R. D., Verploegen, E., Hart, A. J. & Cohen, R. E. Quantitative characterization of the morphology of multiwall carbon nanotube films by small-angle X-ray scattering. *J. Phys. Chem. C* **111**, 5859-5865 (2007).
32. Meshot, E. R. et al. Engineering vertically aligned carbon nanotube growth by decoupled thermal treatment of precursor and catalyst. *ACS Nano* **3**, 2477-2486 (2009).
33. Kim, S. M. et al. Evolution in Catalyst Morphology Leads to Carbon Nanotube Growth Termination. *J. Phys. Chem.* **1**, 918-922 (2010).
34. Xu, M., Futaba, D. N., Yumura, M. & Hata, K. Alignment control of carbon nanotube forest from random to nearly perfectly aligned by utilizing the crowding effect. *ACS Nano* **6**, 5837-5844 (2012).
35. De Volder, M. F. L., Park, S. J., Tawfick, S. H., Vidaud, D. O. & Hart, A. J. Fabrication and electrical integration of robust carbon nanotube micropillars by self-directed elastocapillary densification. *J. Micromech. Microeng.* **21**, 045033 (2011).
36. Chiodarelli, N. et al. Integration and electrical characterization of carbon nanotube via interconnects. *Microelectron. Eng.* **88**, 837-843 (2011).
37. De Volder, M. et al. Diverse 3d microarchitectures made by capillary forming of carbon nanotubes. *Adv. Mat.* **22**, 4384-4389 (2010).
38. Hayamizu, Y. et al. Integrated three-dimensional microelectromechanical devices from processable carbon nanotube wafers. *Nat. Nanotech.* **3**, 289-294 (2008).
39. Deshpande, V. S., Fleck, N. A. & Ashby, M. F. Effective properties of the octet-truss lattice material. *J. Mech. Phys. Sol.* **49**, 1747-1769 (2001).
40. Radford, D. D., Fleck, N. A. & Deshpande, V. S. The response of clamped sandwich beams subjected to shock loading. *Int. J. Impact. Eng.* **32**, 968-987 (2006).

41. Gu, S., Lu, T. J. & Evans, A. G. On the design of two-dimensional cellular metals for combined heat dissipation and structural load capacity. *Int. J. Heat Mass Transfer* **44**, 2163-2175 (2001).
42. TAWFICK, S., DENG, X., HART, A. & LAHANN, J. Nanocomposite microstructures with tunable mechanical and chemical properties. *PCCP*, **12**, 4446-4451 (2010).
43. Novitsky, J. & Miller, C. Wafer-level CSP, wafer-level assembly/test: Integrating backend processes. *Solid State Technol.* **44**, 78 (2001).
44. De Volder, M., Tawfick, S. H., Copic, D. & Hart, A. J. Hydrogel-driven carbon nanotube microtransducers. *Soft Mat.* **7**, 9844-9847 (2011).
45. Hutchison, D. N. et al. Carbon Nanotubes as a Framework for High-Aspect-Ratio MEMS Fabrication. *J. Microelectromech. Syst.* **19**, 75-82 (2010).
46. Zheng, Y., Gao, X. & Jiang, L. Directional adhesion of superhydrophobic butterfly wings. *Soft Matter* **3**, 178-182, doi:10.1039/b612667g (2007).
47. Barth, F. G. How to catch the wind: Spider hairs specialized for sensing the movement of air. *Naturwissenschaften* **87**, 51-58 (2000).
48. Qu, L., Dai, L., Stone, M., Xia, Z. & Wang, Z. L. Carbon nanotube arrays with strong shear binding-on and easy normal lifting-off. *Science* **322**, 238-242 (2008).
49. Rong, Z. et al. Bio-inspired hierarchical polymer fiber-carbon nanotube adhesives. *Adv. Mat.* **26**, 1456-1461 (2014).
50. Lau, K. K. S. et al. Superhydrophobic carbon nanotube forests. *Nano Lett.* **3**, 1701-1705 (2003).
51. Yasuda, S. et al. Improved and Large Area Single-Walled Carbon Nanotube Forest Growth by Controlling the Gas Flow Direction. *ACS Nano* **3**, 4164-4170 (2009).
52. Zhang, Q., Huang, J.-Q., Zhao, M.-Q., Qian, W.-Z. & Wei, F. Carbon nanotube mass production: principles and processes. *Chemsuschem* **4**, 864-889 (2011).
53. Polsen, E. S., Stevens, A. G. & Hart, A. J. Laser printing of nanoparticle toner enables digital control of micropatterned carbon nanotube growth. *ACS Appl. Mater. Interfaces* **5**, 3656-3662 (2013).

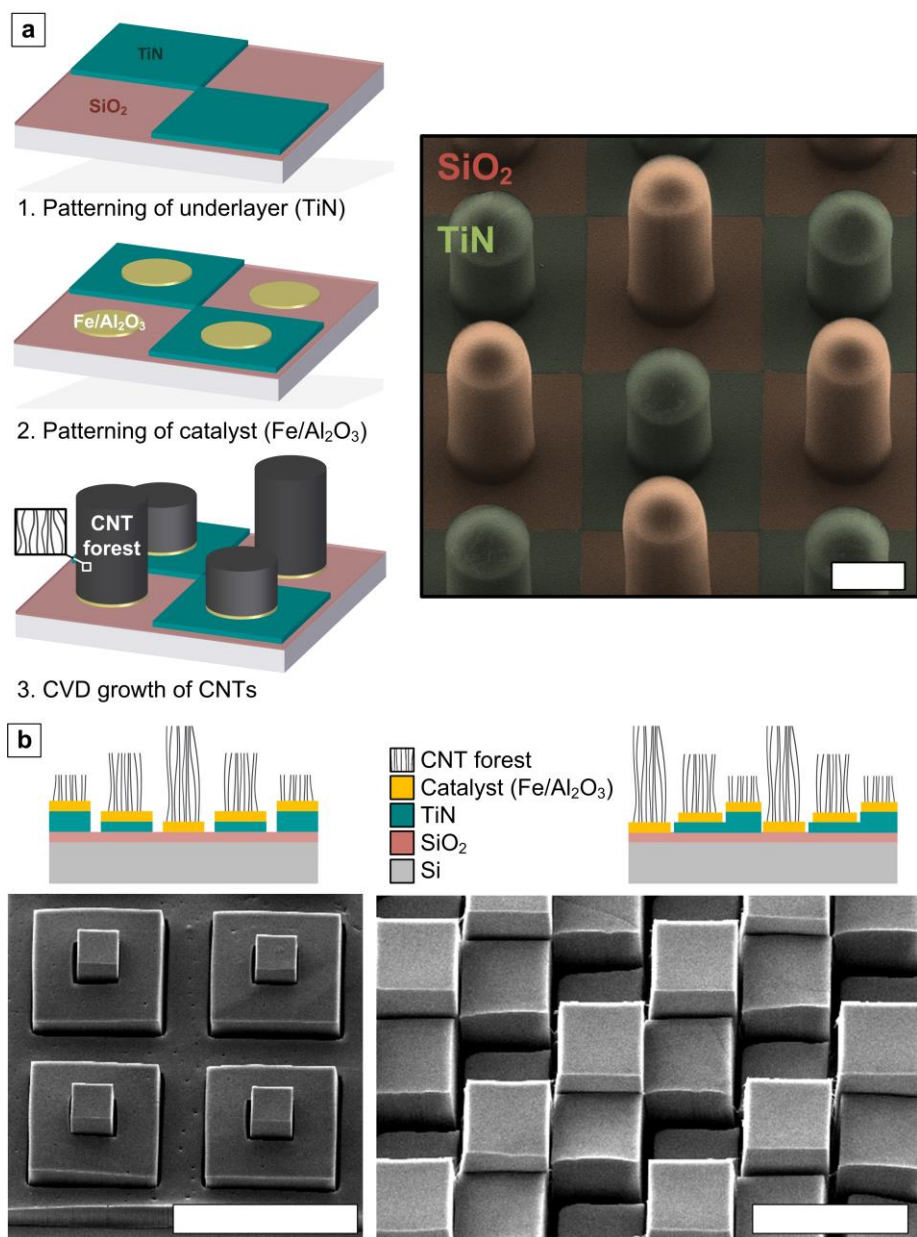


Figure 1. Multi-height CNT micropillar growth using TiN as a rate-controlling catalyst underlayer. (a) Process steps including two lithography steps, and accompanying (color added) pattern of cylindrical CNT micropillars grown on “checkerboard” of alternating TiN (80nm thickness) squares on SiO<sub>2</sub> on the right in a black box. Scale bar is 40 μm (b) Triple-height arrays made by substrate and catalyst patterning with three lithography (TiN layers are 40 nm and 80 nm thickness). Scale bars are 500μm (left) and 200 μm (right).

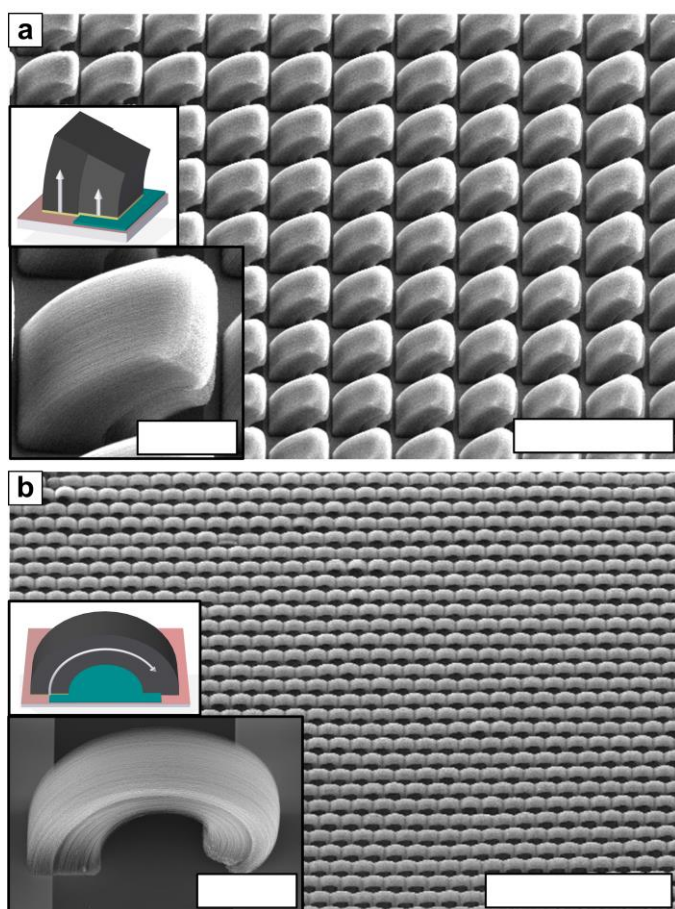


Figure 2. Curved CNT micropillars grown from catalyst rectangles partially overlapping TiN (shown as green layer in the schematics). The pillars bend toward the TiN side, which grows more slowly and couples to the faster-growing region of catalyst directly on SiO<sub>2</sub>. (a) Closely-spaced short structures with  $\sim 45^\circ$  takeoff angle. Scale bars are 100  $\mu\text{m}$  (panel) and 20  $\mu\text{m}$  (inset). (b) Arch-like structures that curve over and contact the substrate at their distal ends. . Scale bars are 200  $\mu\text{m}$  (panel) and 20  $\mu\text{m}$  (inset).

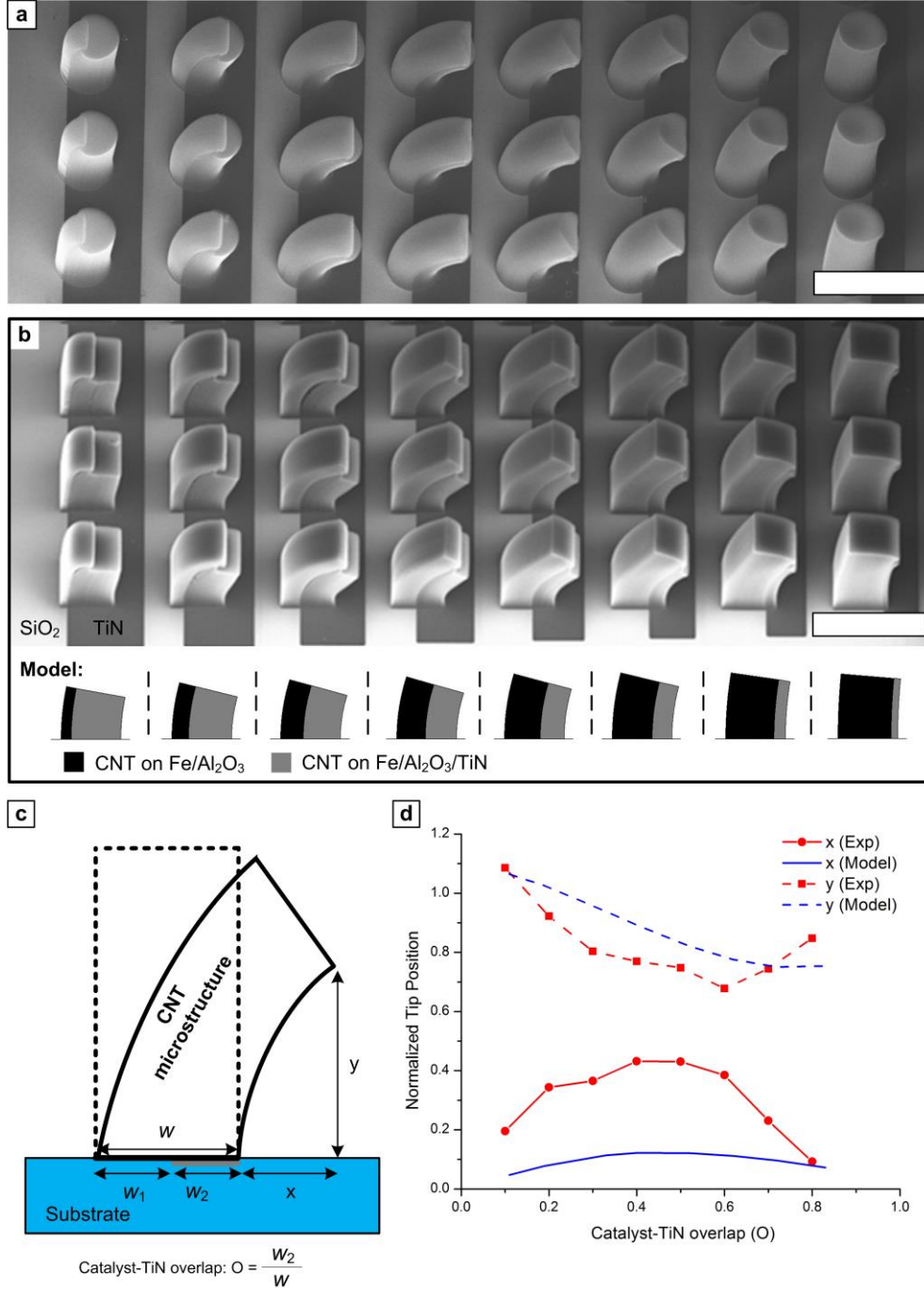


Figure 3. Shape gradients and their use in elementary modeling of the stress-driven CNT growth process. (a,b) arrays of round and square CNT micropillars with decreasing catalyst/TiN overlap from left to right. Scale bars are 100  $\mu\text{m}$ . (c) Schematic of geometric parameters used to quantify deformation of square micropillars. (d) Output of differential expansion model predicting vertical and lateral deflection versus substrate pattern design, comparing simulations, inset to (b), and measurements from SEM images.

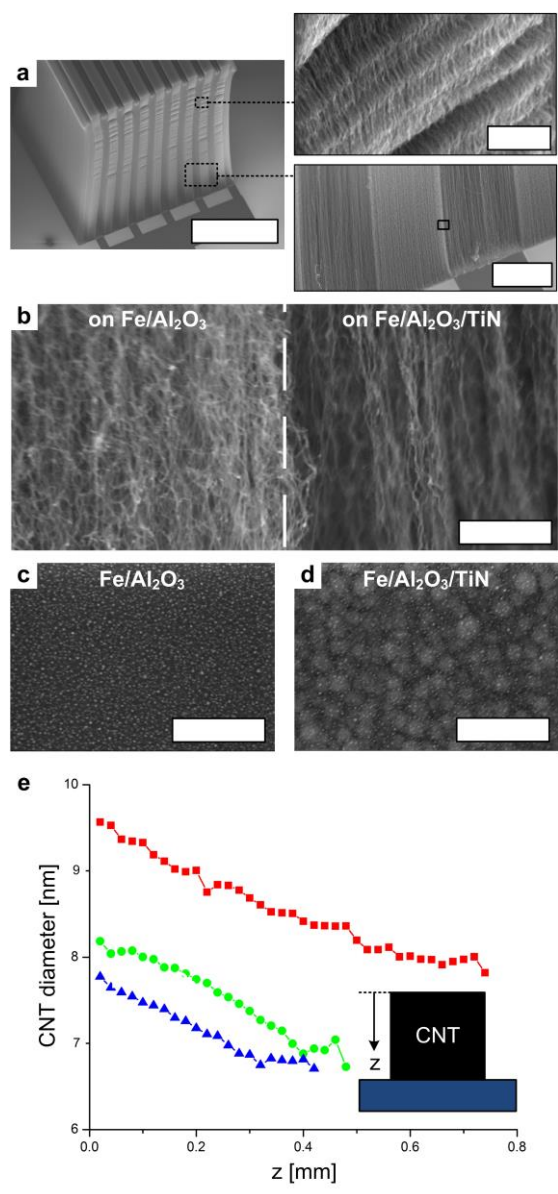


Figure 4. Analysis of CNT morphology. (a) SEM image of micropillar with catalyst on fine stripes of TiN, with close-up images showing the CNT morphology difference and evidence of internal stress causing local deformation. Scale bars are 100 μm (left), 2 μm (upper right) and 10 μm (lower right). (b) Close-up images of the aligned CNT morphology in adjacent segments of the micropillar. Scale bars is 500 nm. (c,d) SEM images of the substrate morphology after annealing in H<sub>2</sub> and rapid cooling, showing hierarchical morphology of nanoparticles on the catalyst/TiN area. Scale bars are 500 nm. (e) Diameter mapping within the CNT forests, from fitting of SAXS data. Red - CNT of Fe/Al<sub>2</sub>O<sub>3</sub>, Green - CNT on Fe/Al<sub>2</sub>O<sub>3</sub>/TiN (40nm), Blue - CNT on Fe/Al<sub>2</sub>O<sub>3</sub>/TiN (80nm).



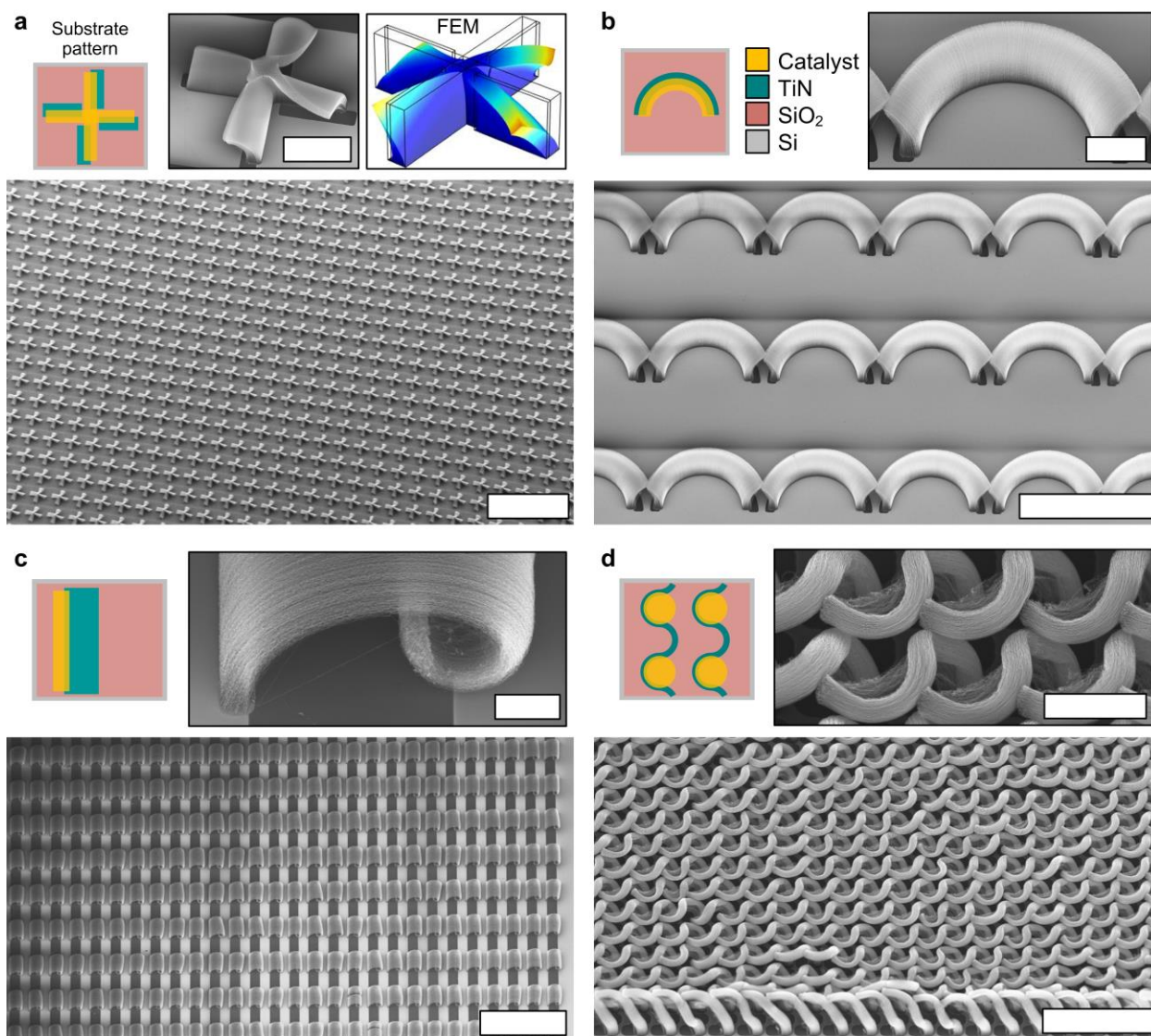


Figure 5. Design and fabrication of arrays of complex microstructures. Each of the four panels contains a sketch (top left) of the catalyst-TiN pattern used for CNT growth, a close-up SEM image (top right), and an exemplary array of structures (bottom). (a) Twisted propeller-like structures, made from azimuthally offset crosshair catalyst/TiN layers, also compared to finite element model (FEM) prediction of shape (top right). Scale bars are 40  $\mu\text{m}$  (top right), and 500  $\mu\text{m}$  (bottom). (b) Outward curving semicircles made from radially offset catalyst/TiN layers. Scale bars are 5  $\mu\text{m}$  (top right), and 100  $\mu\text{m}$  (bottom). (c) Scroll-like deformation of thin-walled microstructures with slight catalyst/TiN overlap. Scale bars are 10  $\mu\text{m}$  (top right), and 250  $\mu\text{m}$  (bottom). (d) Collective organization of bending microstructures into a wavy pattern. Scale bars are 10  $\mu\text{m}$  (top right), and 40  $\mu\text{m}$  (bottom).



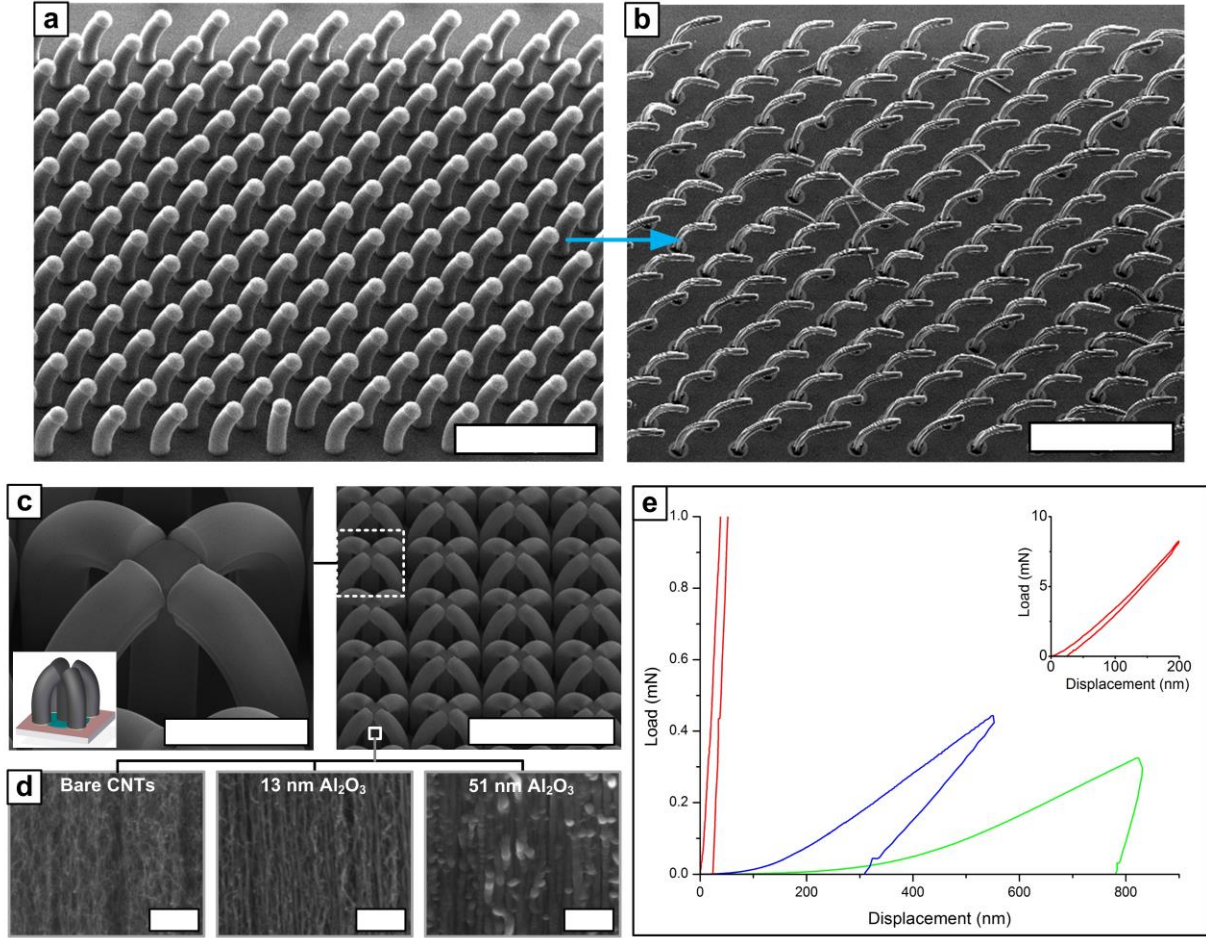


Figure 6. Post-processing of 3DCNT microstructures. (a,b) Array of bending micropillars before and after capillary forming, respectively. The unidirectional anisotropic morphology is maintained and the micropillar cross section decreases, while the lateral deflection angle of the structures increases. Scale bars are 200  $\mu\text{m}$ . (c) Microtruss array fabricated to study mechanical reinforcement by vapor-phase coating of the CNTs. Scale bars are 100  $\mu\text{m}$  (left) and 400  $\mu\text{m}$  (right). (d) SEM images of aligned CNTs in the forest sidewall before and after coating with  $\text{Al}_2\text{O}_3$  by ALD. Scale bars are 1  $\mu\text{m}$ . (e) Load-displacement curves before and after ALD coating, where the stiffness is measured from the slope of the unloading curve. Green – No coating, Blue –  $\text{Al}_2\text{O}_3$  coating (ALD, 100 cycles), Red –  $\text{Al}_2\text{O}_3$  coating (ALD, 1000 cycles).

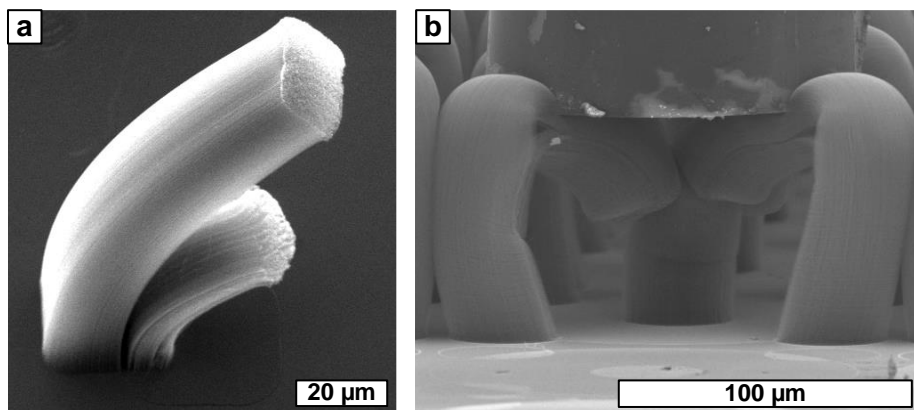


Figure S1. SEM image of a CNT microstructure where the fast (on Fe/Al<sub>2</sub>O<sub>3</sub>/SiO<sub>2</sub>) and slow (on Fe/Al<sub>2</sub>O<sub>3</sub>/TiN/SiO<sub>2</sub>) growing portions delaminated completely at the vertical interface. (b) In-situ SEM indentation of a CNT micro-truss. The curved beams do not split apart even after a large deformation, except locally near the center where the large deformation causes kinking.

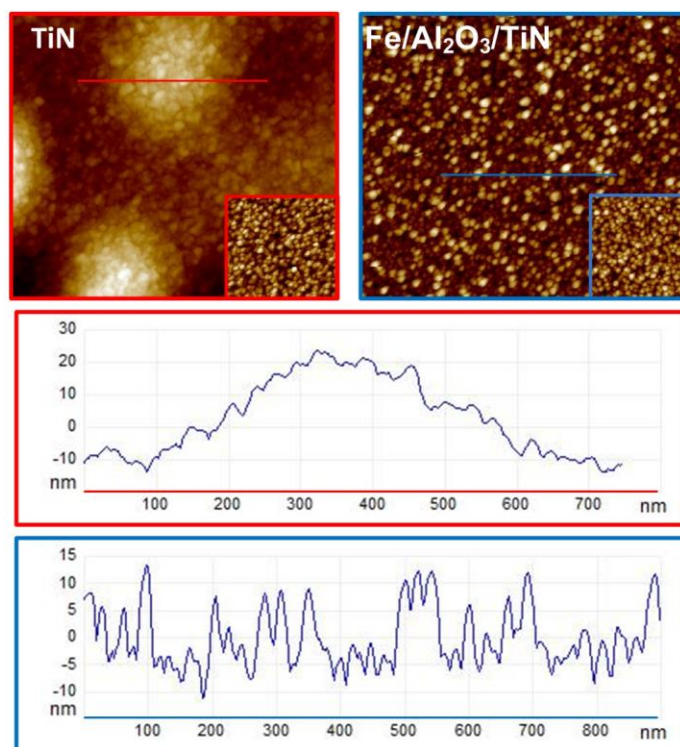


Figure S2. AFM images comparing topography of annealed TiN layer, and Fe/Al<sub>2</sub>O<sub>3</sub> catalyst on TiN. Images show that TiN layer roughens when annealed with features that are 100s of nanometers wide and 10s of nanometers high (red). Annealed catalyst over TiN layer shows catalyst particles on larger scale mounds (blue). The insets show AFM scans before annealing.

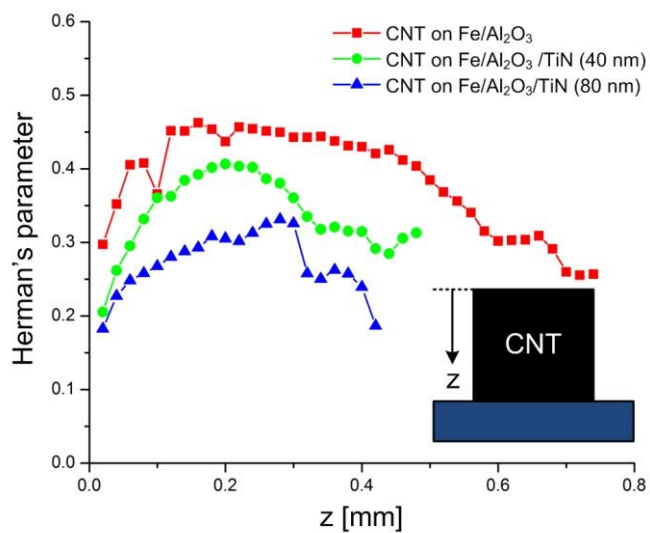


Figure S3. Herman's parameter mapping within the CNT forests, from fitting of SAXS data.

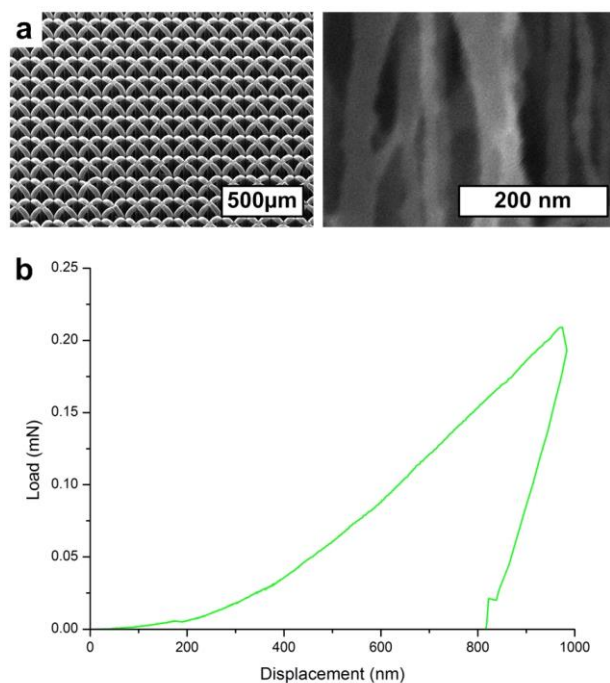


Figure S4. Parylene-coated CNT microtrusses for mechanical reinforcement. (a) Overview and close up SEM images of the coated CNT trusses. (b) load-displacement curve of a single microtruss with identical geometry as Al<sub>2</sub>O<sub>3</sub>-coated trusses shown in the main text.

## Chapter 4: Scaling the stiffness, strength, and toughness of ceramic-coated nanotube foams into the structural regime

*Contents of this chapter have been published as: A. Brieland-Shoultz, S. Tawfick, S.J. Park, M. Bedewy, M. Maschmann, J.W. Baur and A.J. Hart, "Scaling the stiffness, strength, and toughness of ceramic-coated nanotube foams into the structural regime." Adv. Funct. Mater. **24**, 5728-5735 (2014).*

### Introduction

Design of the hierarchical structure and composition of cellular materials offers a versatile means to tune mechanical properties, such as Young's modulus, strength, and toughness. Cellular materials can also achieve unique combinations of properties, while maintaining large surface areas and low mass density. For example, the mechanical properties of metallic foams enable their use for energy absorption in consumer goods packaging and composite sandwich structures, and their porosity enables use as battery and capacitor electrode supports <sup>1</sup>. Ceramic foams are widely used as mechanical, thermal and acoustic insulators, for flow filtration and regulation, and as catalyst supports <sup>2</sup>. Many natural materials use analogous design principles; for example, the exquisite structure-function relationship of bone spans from stiff and dense cortical load bearing bone to highly porous cancellous bone where haematopoiesis occurs <sup>3</sup>. Further, the geometric and compositional hierarchy of soft and hard constituents result in the high toughness of bone at low mass density <sup>4</sup>.

Recently, micro- and nanofabrication methods such as photo, X-ray, and interference lithography have been applied to prototype micro- and nanoscale foams with unique cell geometries and hierarchical structures <sup>5</sup>. For example, fabrication of epoxy lattices by interference lithography enabled *a priori* tuning of the cell size in the sub-micron regime. These foams showed a classical power-law relationship between Young's modulus and relative density ( $E \sim [\rho/\rho_s]^n$ ), with  $n=1.26$ ; at  $\rho_r = 0.5$  the energy absorption reached  $4 \text{ J/cm}^3$  at strain  $< 0.25$  <sup>5</sup>. Use of sacrificial polymer templates to make hollow tube metallic microlattices resulted in a foam with record low density ( $\rho_r = \rho/\rho_s = 2 \times 10^{-4}$ ,  $\rho \sim 1 \text{ mg/cm}^3$ ) and high recoverability, but low Young's modulus ( $E \sim 550 \text{ kPa}$ ) <sup>6</sup>. In this case, due to the hollow structure of the metal truss members, the relationship between modulus and relative density followed a power law with  $n=2$ . This contrasts most fibrous nanoscale aerogels and foams, having  $n=2-3$ , which is attributed to

low connectivity between the constituent struts <sup>7</sup>. When comparing foam materials, a higher power law exponent results in a relatively larger change in  $E$  for the same change in density.

While these methods have enabled exploration of new design and property regimes for engineered foams, their manufacturing cost and complexity currently prohibit them from scaling to large quantities that can be incorporated in macroscale engineering systems. In contrast, most industrially manufactured foams have isotropic and random cell geometry. Closed cell metallic and polymer foams are usually manufactured by gas injection into melts, while open cell metallic foams are usually made by vapor deposition or electrodeposition of metal precursors on polymer scaffolds. Porous metallic and ceramic materials can also be manufactured by compaction and sintering of powders <sup>8</sup>.

Directed growth and self-organization of nanostructures is emerging as an attractive and potentially scalable route to create hierarchical materials having both composition- and geometry-derived mechanical properties. Carbon nanotubes (CNTs) have outstanding properties including high Young's modulus, strength, conductivity, and thermal stability. Moreover, CNTs can be manufactured in large quantities by cost-effective chemical vapor deposition (CVD) methods <sup>9</sup>, and assembled, either during or after CVD, into ordered forms such as vertically aligned "forests", yarns, and sheets <sup>10</sup>. While as-grown CNT forests have high compressibility <sup>11</sup>, <sup>12</sup> and have shown promise as energy-dissipating surfaces and interlayers <sup>11, 13</sup>, CNT forests and isotropic foams made from CNTs <sup>13</sup> have low density usually in the range of 10-100 kg/m<sup>3</sup> or  $\rho/\rho_s = 0.5\text{-}5\%$  (considering  $\rho_s$  to be equal to solid graphite at 2200 kg/m<sup>3</sup>).

Therefore, it remains an opportunity to explore how self-assembly of CNTs, in combination with conformal coating methods <sup>14</sup>, can be used to create bulk materials with efficient and widely tunable properties, and to compare these properties to commercially available structural materials. In this study, we show that nanoscale coating of a ceramic onto clean CNT forests enables unprecedented tuning of Young's modulus, strength, and toughness, without changing the structure or composition of the nanoporous material.

## Methods

*CNT growth:* The catalyst for CNT forest growth is deposited on a (100) silicon wafer with 300 nm of thermally grown silicon dioxide. Photoresist (SPR220) is patterned by photolithography and developed, and then films of 10 nm Al<sub>2</sub>O<sub>3</sub> and 1 nm Fe are deposited by sputtering (Kurt J.

Lesker PVD Lab 18). The photoresist is removed by performing two consecutive cycles (8 minutes each) of ultrasonication in acetone, followed by flushing with IPA. CNT growth is performed by thermal CVD in a quartz tube furnace (Thermo-Fisher Minimate, 22 mm inner diameter). Pieces of the patterned catalyst wafer are placed in the quartz tube and sealed, and then the furnace is flushed with 1000 sccm He for 5 minutes. Then 100/400sccm H<sub>2</sub>/He is flowed for 20 minutes; the temperature is ramped up to 775°C during the first 10 minutes and held for the next 10 minutes. For CNT growth, 100 sccm C<sub>2</sub>H<sub>4</sub> is added to the gas mixture while the temperature is maintained at 775°C. Once the growth step is complete, the furnace power is turned off, and the tube is flushed with 1000 sccm He until the furnace is below 100°C. The height of the CNT microstructures was controlled by the growth time, with the growth rate equaling approximately 50 µm/minute.

*ALD coating:* After growth, CNT micropillars were coated with alumina deposited via atomic layer deposition (ALD). The ALD process is performed in a low pressure CVD chamber (Oxford OpAl) at 300 mTorr and 150°C via alternating pulses of Al(CH<sub>3</sub>)<sub>3</sub> and H<sub>2</sub>O with a purge between the pulses.

*Mechanical testing:* Micropillars and perforated forests were tested in compression using a MTS Nanoindenter XP with flat diamond punch (100 µm diameter). In situ SEM compression tests were performed using a flat nanoindentation tip (100 µm diameter) within a custom-built micromechanical test frame inside a SEM (FEI QUANTA ESEM), as described by Maschmann et al <sup>11</sup>.

*X-ray scattering:* As-grown CNT micropillars as well as Al<sub>2</sub>O<sub>3</sub>-coated micropillars were mounted on a motorized sample stage in the Synchrotron X-ray beamline. Energy of the X-ray beam used was 10 +/- 0.1 keV. Scattering patterns were collected on a 2D area detector. The size of the X-ray beam was controlled using a pair of motorized precision slits. More details of the experimental setup and the data analysis techniques are published in Bedewy et al <sup>19</sup>.

## **Results and Discussion**

### *Fabrication and compression testing of ceramic-carbon nanotube foams*

First, CNT forests, comprising vertically aligned multi-wall CNTs, were synthesized from a supported metal catalyst film (see Methods) by atmospheric pressure chemical vapor deposition (CVD) <sup>15</sup>. Then, Al<sub>2</sub>O<sub>3</sub> was deposited by atomic layer deposition (ALD), conformally coating

the CNTs and CNT bundles within the forest, resulting in a nanoporous composite with ceramic-carbon core-shell structural members. The thickness of  $\text{Al}_2\text{O}_3$  on the CNTs was controlled by the number of ALD process cycles. During each cycle of ALD, the precursors ( $\text{Al}(\text{CH}_3)_3$  and  $\text{H}_2\text{O}$ ) are sequentially introduced in two half-reaction stages, and the thickness during each cycle is self-limiting to approx.  $1.3 \text{ \AA}$  <sup>16</sup>.

The change in morphology of the CNTs due to  $\text{Al}_2\text{O}_3$  coating is shown in Fig. 1a-c. First, ALD  $\text{Al}_2\text{O}_3$  nucleation occurs preferentially at surface defects on the CNTs (Fig. SI1) <sup>17</sup> and at contact points among CNTs. After nucleation, the coating grows to fully cover the individual CNTs, and in some cases bundles of CNTs. After a certain thickness the coated CNTs and bundles coalesce. Judging from SEM images of the forest sidewalls, this coalescence begins at coating thickness of approximately 30 nm, compared to the average CNT-CNT spacing of approximately 50 nm (number density  $\sim 3 \times 10^{10}/\text{cm}^2$ ). The local CNT spacing and density represent a distribution, determined by the waviness and bundling of the CNTs which can be approximated by their average orientation angle as discussed later.

CNT micropillars, made using a lithographically patterned catalyst, were used to study the scaling of mechanical properties with the number of ALD cycles, and to relate the mechanics to the penetration depth of ALD coating. Test samples were fabricated with arrays of CNT micropillars having radii ranging from 10-35  $\mu\text{m}$  (Fig. 1d). The micropillars were tested in quasi-static axial compression using a nanoindenter with a cylindrical flat diamond tip (50  $\mu\text{m}$  radius). The Young's modulus was obtained from the unloading slope in continuous modulus mode (10 nm oscillations at 50 Hz) at a compressive pre-strain of 0.05 (approximately 2  $\mu\text{m}$  compression of the micropillar).

Load-displacement curves of individual 15  $\mu\text{m}$  radius  $\text{Al}_2\text{O}_3$ -CNT micropillars with 30  $\mu\text{m}$  height, with coatings of 0, 100, and 1000 ALD cycles, are compared in Fig. 1e. The load capacity of the pillars increases from  $<0.1 \text{ mN}$  for the uncoated (bare CNT) pillar, to 0.7 mN with 13 nm coating (100 ALD cycles), and 130 mN with 51 nm coating (1000 cycles). As shown in Fig. 2c for  $R_{\text{pillar}} = 15 \text{ \mu m}$ , the Young's modulus scales from 14.5 MPa for uncoated CNTs to 24.5 GPa with 51 nm coating.

#### *Structural characterization of coating morphology*

To further understand the structure-property relationship via ALD coating, we measured the coating thickness and the density evolution per ALD cycle. To determine the penetration depth, we coated patterned CNT forest “line” features and found, as shown in Fig. 3a, that the penetration depth is approximately 5-7  $\mu\text{m}$ . To overcome this limitation and demonstrate the scaling on large sample areas, perforated “honeycomb” patterns (Fig. 3b) with 10  $\mu\text{m}$  spacing between holes were synthesized. The perforations enabled uniform ALD coating throughout the CNT forest, and therefore were used for subsequent characterization.

Transmission SAXS was then used to characterize the morphology of the as grown and  $\text{Al}_2\text{O}_3$ -coated CNTs by placing the honeycomb film sample in the beamline path of a synchrotron X-ray beam and collecting the scattered X-rays on an area detector (Fig. 4, S2)<sup>18, 19</sup>. As in our previous work<sup>19</sup>, the statistical distribution of outer diameters for both coated and uncoated CNTs was obtained by fitting a mathematical model of polydisperse core-shell cylinders to line-scans of scattering intensity. This determines the average outer and inner radii of the bare CNTs as 5.0 and 3.5 nm, respectively. The linescans are obtained by integration of the scattered intensities within a sector of  $\pm 10^\circ$  about the axis of maximum intensity on the 2D scattering pattern, as shown in Fig. S2. As seen in Fig. 4a, the peak corresponding to the scattering from the population of  $\text{Al}_2\text{O}_3$ -coated CNTs shifts to a lower value on the x-axis with increasing coating thickness. This indicates a significant increase in the size of the scatters, which is quantified by fitting the data for coated samples with a core-shell scattering model. Analysis of the coated samples gives average coating thickness of 8.5, 14.5 and 26.7 nm for 50, 100 and 200 cycles of ALD, (Fig. 4b). For 100 and 200 cycles, a second peak on the SAXS linescans is seen at a  $q$  value higher than the form-factor peak. This peak could arise from the observed roughening of the  $\text{Al}_2\text{O}_3$  layer at the greater coating thickness (Fig. S2c).

We also estimated the average coating thickness by measuring the weight of the samples before and after ALD coating. We found a sub-linear relationship between mass and the number of cycles, showing that the deposited thickness per ALD cycle is affected by the ability of the precursors to diffuse into the CNT forest; this reduces as the porosity of the sample decreases when subject to multiple cycles. We therefore constructed a model where the pore size is decreased with each subsequent cycle. We found (Fig. 4b) that the best fit to the SAXS and weight measurements corresponds to a decrease of effective diffusion coefficient of vapor phase precursors in porous media by 0.5% per cycle, starting at the 140<sup>th</sup> cycle of ALD coating. We



did not consider the increase in available area due to the increase in effective diameter, which is counteracted by the coalescence of coated CNTs as the coating thickness increases. Improved uniformity of coating could likely be achieved by increasing the precursor cycle duration.

As a result of diffusion-limited coating, the Young's modulus of the  $\text{Al}_2\text{O}_3$ -CNT composites depended strongly on the micropillar diameter. The full matrix of compression tests performed with pillars having 10-35  $\mu\text{m}$  radius, at each coating thickness, is summarized in Fig. S3. Here, modulus is inversely proportional to pillar diameter, as the reinforcement of larger pillars is limited by ALD penetration and therefore the final composite pillar is a reinforced shell surrounding a soft core of uncoated CNTs. These trends, and specifically the size-dependent modulus of non-coated pillars, are also attributed to size-dependent growth effects on the density of CNTs within the forest. This topic is currently under separate study in our group <sup>20</sup>.

### *Model of cellular mechanics*

We now develop a model of the Young's modulus of the  $\text{Al}_2\text{O}_3$ -CNT composites under quasi-static loading. First, as verified by SAXS, we note that ALD coating creates a nanoporous composite where the load-bearing elements are nanoscale core-shell beams. These beams are loaded primarily in bending when the structure is subject to compressive loading. Previous work using *in situ* SEM digital image correlation has shown that the CNT-CNT contact points within an uncoated CNT forest do not slip upon compressive loading to strains below the failure threshold of approximately 5% local strain <sup>21</sup>. As a result, uncoated CNT forests can be approximated as open-cell foams where the deformation of individual CNTs and bundles represent the cell walls.

We approximate the nanoporous network of interconnected wavy  $\text{Al}_2\text{O}_3$ -CNT beams as an effective cellular solid with rectangular unit cell geometry (Fig. 2a). We consider the CNTs as an array of beams loaded simultaneously in bending and compression <sup>22</sup>, having identical diameter and length. We further use SAXS to determine the average orientation angle of each CNT with respect to the vertical axis ( $\theta = 40^\circ$ , with a random distribution of azimuthal angles) <sup>23</sup>, giving the unit cell aspect ratio ( $H_{\text{CNT}}/W_{\text{cell}} = 1.67$ ). Although the CNT alignment and therefore the orientation are known to vary throughout the forest due to changes in the CNT density, here we use a single average value to represent the effective properties.

With this information, we first calculate the effective unit cell size, where each unit cell contains one angled CNT having length ( $L_{CNT}$ ) and inclination angle ( $\theta$ ). This is an approximation for the real structure of the forest, which certainly contains a distribution of CNT angles, effective lengths, and effective unit cell sizes. The stiffness of a unit cell  $k_{CNT}$  is represented by a cantilever beam in combined axial compression and end-loaded cantilever beam bending (Fig. 2a,b),

$$\frac{1}{k_{CNT}} = \frac{\sin^2 \theta}{E_{CNT} I_{CNT}} L_{CNT}^3 + \frac{\cos^2 \theta}{E_{CNT} A_{CNT}} L_{CNT} \quad (\text{Eq. 1})$$

Here,  $E_{CNT}$  is the Young's modulus (1 TPa<sup>24</sup>, based on the wall area only), and the cross-sectional area of the CNT ( $A_{CNT}$ ) and second moment of area ( $I_{CNT}$ ) are both determined from the average CNT outer and inner diameters measured by SAXS. The total stiffness of the foam is therefore related to the unit cell stiffness by the assembly of  $M$  (across the horizontal cross-section) by  $N$  (along the height) unit cells (Fig. 2a) into a cylindrical solid representing a micropillar,

$$k_{assembly} = \frac{\pi E_{pillar} R_{pillar}^2}{H_{pillar}} = \frac{M k_{CNT}}{N} \quad (\text{Eq. 2})$$

We derive  $L_{CNT} = 210$  nm, as well as  $N$  and  $M$ , which give  $h = 160$  nm and  $w = 95$  nm.

We now predict the modulus of the composite assuming uniform coating of the slanted CNTs within each unit cell, causing a proportional contribution of each cell to the overall stiffness of the micropillar structure. Therefore, we then scale the Young's modulus of the unit cell, using a core-shell beam model where the  $\text{Al}_2\text{O}_3$  shell thickness is determined by the number of ALD cycles. The  $\text{Al}_2\text{O}_3$  Young's modulus is taken to be 180 GPa<sup>25</sup>.

$$(EI)_{composite} = E_{CNT} I_{CNT} + E_{Al_2O_3} I_{Al_2O_3} \quad (\text{Eq. 3})$$

We used  $E_{CNT}$  equal to The comparison between the measured compressive modulus and the predicted modulus from the unit cell model is shown in Fig. 2c. For coating thickness below ~5 nm, the effective spring model with constant  $L_{CNT}$  closely predicts the experimentally measured scaling of elastic modulus with coating thickness. As a result, we conclude that the primary mechanism of axial deformation of the foam is bending of the individual nanoscale elements. However, to our surprise, assuming constant  $L_{CNT}$  does not accurately predict the measured stiffness at coating thickness >10 nm. This is because the length of the slanted core-

shell beams decreases as more coating is deposited, causing additional junctions to form between nearby CNTs whose gaps are filled by the thicker coating. To adapt the model to the morphology evolution, we iteratively update the characteristic length,

$$L_{CNT|n+1} = L_{CNT|n} - 2t_{n+1}.$$

Here,  $n$  and  $n+1$  are the cycle numbers, and  $t$  is the  $\text{Al}_2\text{O}_3$  deposition thickness during the cycle, which is determined from the SAXS and density analysis. This is schematically shown in Fig. 2d. The variable  $L_{CNT}$  model accurately predicts the modulus scaling at large coating thickness, up to the maximum coating of 51 nm. At this point, the increased reinforcement due to coalescence of individual CNTs and bundles (as seen in Fig. 1c) changes the effective unit cell height, thus increasing load transfer by compression of the structural members rather than bending. Moreover, further increase in density of the composite is limited, as we suspect the exterior voids are fully closed and the coating precursors can no longer penetrate uniformly and deeply into the foam. As a result, we calculated the Young's modulus to represent ALD penetration depth of 5  $\mu\text{m}$  from the outside surfaces of the micropillar. In Fig. S4 we provide plots showing the dependence of Young's modulus on the ALD penetration depth.

While penetration of larger micro-scale geometries is limited under the present ALD conditions, the perforated honeycomb design (Fig. 3c) shows potential to achieve uniform composite properties over large areas, as it enables uniform infiltration of the coating precursors. A honeycomb CNT forest with 1000 cycles ALD  $\text{Al}_2\text{O}_3$  has  $E = 38.3 \pm 3.7$  GPa based on the solid area of the cross-section. Nevertheless, future study should focus on optimizing the depth and uniformity of infiltration and coating, as determined by the deposition temperature, pressure, and the precursor chemistry.

The  $\text{Al}_2\text{O}_3$ -CNT foams also withstand large deformations at high stresses before failure, and therefore have exceptional toughness. In Fig. 5 we show the measured stress versus energy absorbed for foams with selected coating thicknesses. The data here is obtained by integrating the area under the quasi-static stress-strain curves of micropillars compressed to large strains. We note three regions, as compressive strain increases: (1) a linear regime where the energy absorbed is proportional to the applied stress; (2) a steep increase in energy absorbed, corresponding to the plateau in the stress-strain curve; and (3) densification as the material fails. Large energy absorption, characterized by an increase in total energy stored due to deformation without much increase in the resultant stress, occurs until the vertical tip of each of these curves

before the slope is decreased due to the small resultant strain at the foam densification regime (3). This indicates that most of the energy absorbed is due to the large deformations of the individual cells, a favorable property for structural foams.

The high toughness indicates that the CNTs, even at very low weight % (~2.5 wt% CNTs after 1000 cycles ALD), bridge cracks in the  $\text{Al}_2\text{O}_3$  foam that form upon compressive loading. This prevents catastrophic fracture until a very large strain, and hence results in large energy absorption. We believe that rapid crack propagation is mitigated due to the collective buckling of the  $\text{Al}_2\text{O}_3$ -CNT struts held in proximity by van der Waals interactions, or in some areas by thin ceramic junctions. In contrast, classical open cell (e.g., Al) foams have continuous uniform struts connected at the junctions and spanning the cells. Thus, at the same density, classical foams require larger forces to buckle the members, and exhibit a narrower plateau in the stress-strain curve than observed for the  $\text{Al}_2\text{O}_3$ -CNT foams.

The deformation and failure mechanisms are further understood by examining in situ SEM videos of micropillars under compression (Fig. 5b). In these videos and the accompanying stress-strain curves, we find that foams with approximately 10 nm  $\text{Al}_2\text{O}_3$  coating fully recover large compressive strains, and exhibit significant hysteresis (i.e., material damping). We suspect this is due to a balance between the reinforcement provided by the  $\text{Al}_2\text{O}_3$  coating, enabling the elastic energy to reversibly overcome the stiction of the struts due to van der Waals forces, while remaining flexible to prevent fracture at large global strains. At thinner coatings, the applied stress is not recovered as stiction dominates, whereas at thicker coatings, fracture occurs, resulting in permanent deformation albeit with very high toughness. The role of the coating thickness in joining and bundling CNTs into a hierarchical nanocomposite structure is evident by comparing the fracture behavior of pillars in the thick coating regime. The pillar with 28 nm coating splits outward as fracture propagates parallel to the CNTs, while the pillar with 43 nm coating initially cracks then crushes uniformly under uniaxial compression.

In summary of the above data, we achieve tuning of the elastic modulus by more than 1000-fold by simply varying the thickness of the  $\text{Al}_2\text{O}_3$  ALD coating. The achieved values (Fig. 5a) range from (on the low end) those typical of uncoated CNT foams and other low-density nanostructured foams, to (on the high end) those known for structural aluminum honeycombs having millimeter-scale cell size<sup>26</sup>. Moreover, the strength of our  $\text{Al}_2\text{O}_3$ -CNT composites, which is determined as the maximum stress before the slope of the loading curve decreases

abruptly (Fig. 5b, Fig. S5), is 10-fold higher than isotropic aluminum foams having the same density of  $\rho = 1000 \text{ kg/m}^3$ , and at this point is comparable to compact bone which has 2-fold higher density ( $\rho = 2000 \text{ kg/m}^3$ )<sup>3</sup>. The modulus that we achieve also exceeds that measured for composites of mechanically densified CNT forests with aerospace grade epoxy, where  $E = 9 \text{ GPa}$  is achieved at 20% CNT volume fraction<sup>27</sup>. As stated before,  $E$  is defined as the slope of the unloading curve, and  $\sigma_y$  is defined as the location on the stress-strain curve where the slope starts to decrease after the initial linear-elastic regime.

Comparing the scaling behavior to conventional open cell foams, we note that the Young's modulus and strength of the  $\text{Al}_2\text{O}_3$ -CNT composite scale as  $E \sim \rho^{2.8}$  and  $\sigma_y \sim \rho^{2.9}$  (Fig. 5a,b). Ideal bend-dominated open-cell foams such as open-cell polymer foams<sup>28</sup>, and aluminum honeycombs<sup>29</sup> scale as  $E \sim \rho^2$  and  $\sigma_y \sim \rho^2$ . The modulus scaling of our ALD-coated CNTs incidentally resembles the Young's moduli of isotropic CNT foams<sup>30</sup>, CNT aerogels<sup>31</sup>, and Si aerogels<sup>32</sup> which scale as  $\sim \rho^3$ , and commonly attributed to the interdependence of strut thickness and cell size. This explains the discrepancy between the measured  $E$  and the constant length strut analytical model (Fig. 2c). On the other hand, ultralight open-cell foams such as Ni-P microlattices<sup>6</sup> show  $E \sim \rho^2$  because of the strut aspect ratio is independent of density. High modulus scaling power ( $n$ ), as shown by the  $\text{Al}_2\text{O}_3$ -CNT foams, is advantageous because we begin with low-density as grown CNTs and achieve a comparatively large increase in mechanical properties with increasing density. The controllability and interdependence of stiffness, strength, and toughness will certainly depend on the initial CNT density, diameter, and morphology, and moreover on the crystallinity and composition of the coating. Further study is warranted to understand these phenomena, and to engineer the mechanical energy storage and dissipation properties

In the present study, the scale of the materials tested was limited to the honeycomb films covering  $\sim 1 \text{ cm}^2$  area, and this area is determined by the size of the CVD furnace used for CNT growth. Nevertheless, the design principles of conformal coating and hierarchical patterning could be realized on much larger scales, such as within coatings of CNTs grown on woven micro-fibers or other porous frameworks<sup>33</sup>. Moreover, emerging methods to pattern CNT growth catalyst using continuous printing methods such as laser printing<sup>34</sup>, and machines for roll-to-roll CVD on metal foils, suggest that large-area coating and lamination of CNT forests

will be possible in the future. Several schemes for high-speed continuous ALD have also been reported and are being commercialized<sup>35</sup>.

## **Conclusion**

Conformal coating of CNT forests may serve as a scalable platform for the engineering and fabrication of hierarchical foams with nanoscale cell geometry. As demonstrated here, Al<sub>2</sub>O<sub>3</sub>-CNT foams made using lithographically patterned CNT microstructures followed by ALD coating show 1000-fold tunable Young's modulus, compressive strength, and toughness; and the scaling of Young's modulus over this wide range can be accurately predicted by the mechanics of beam deformation as informed by X-ray characterization of the coating thickness. Moreover, the Al<sub>2</sub>O<sub>3</sub>-CNT foams have ~10-fold higher strength than commercial aluminum foams at the same density, as well as higher toughness due to the high ductility exhibited by the nanostructured ceramic coating. As a result, these foams may be suitable for filtration and shock absorption under high temperature and pressure conditions. We believe that capabilities to grow and coat CNTs in hierarchically microstructured geometries, on advanced fibers, and within porous materials, will enable realization of core-shell CNT-based foams in a wide range of macroscopic configurations. Future exploration of both ceramic and metallic coatings could enable new high-performance foams for structural applications as well as electrochemical energy storage materials where porosity and mechanical robustness are essential to high performance.

## **Acknowledgements**

This work was supported by the Air Force Office of Scientific Research (Young Investigator Program, FA9550-11-1-0089), the Office of Naval Research (Young Investigator Program, N000141210815), and the Defense Advanced Research Projects Agency (HR0011-10-C-0192). Support from DARPA was received under Agreement to NextGen Aeronautics, and any opinions, findings, and conclusions or recommendations expressed in this material do not necessarily reflect the views of NextGen Aeronautics and/or DARPA. Microfabrication was performed at the Lurie Nanofabrication Facility (LNF), which is a member of the National Nanotechnology Infrastructure Network (NNIN); and electron microscopy was performed at the Michigan Electron Microbeam Analysis Laboratory (EMAL). SAXS was performed at the G1 beamline at the Cornell High Energy Synchrotron Source (CHESS) at Cornell University, which is supported

by supported by the National Science Foundation and the National Institutes of Health under Grant DMR-0225180.

## References

1. R. Verdejo, R. Stämpfli, M. Alvarez-Lainez, S. Mourad, M. A. Rodriguez-Perez, P. A. Brühwiler, M. Shaffer. Enhanced acoustic damping in flexible polyurethane foams filled with carbon nanotubes. *Compos. Sci. Technol.* **69**, 1564-1569 (2009); H. N. G. Wadley. Cellular metals manufacturing. *Adv. Eng. Mater.* **4**, 726-733 (2002); D. T. Queheillalt, D. D. Hass, D. J. Sypeck, H. N. Wadley. Synthesis of open-cell metal foams by templated directed vapor deposition. *J. Mater. Res.* **16**, 1028-1036 (2001).
2. A. Barty, S. Marchesini, H. N. Chapman, C. Cui, M. R. Howells, D. A. Shapiro, A. M. Minor, J. C. H. Spence, U. Weierstall, J. Ilavsky, A. Noy, S. P. Hau-Riege, A. B. Artyukhin, T. Baumann, T. Willey, J. Stolken, T. van Buuren, J. H. Kinney. Three-dimensional coherent x-ray diffraction imaging of a ceramic nanofoam: Determination of structural deformation mechanisms. *Phys. Rev. Lett.* **101**, 055501 (2008).
3. L. J. Gibson, M. F. Ashby, *Cellular Solids: Structure and Properties*, Cambridge University Press (1999).
4. R. O. Ritchie. The conflicts between strength and toughness. *Nat. Mater.* **10**, 817-822 (2011).
5. J.-H. Lee, L. Wang, M. C. Boyce, E. L. Thomas. Periodic bicontinuous composites for high specific energy absorption. *Nano Lett.* **12**, 4392-4396 (2012).
6. T. A. Schaedler, A. J. Jacobsen, A. Torrents, A. E. Sorensen, J. Lian, J. R. Greer, L. Valdevit, W. B. Carter. Ultralight metallic microlattices. *Science* **334**, 962-965 (2011).
7. K. H. Kim, Y. Oh, M. F. Islam. Mechanical and thermal management characteristics of ultrahigh surface area single-walled carbon nanotube aerogels. *Adv. Funct. Mater.* **23**, 377-383 (2013).
8. R. M. German, *Sintering Theory and Practice*, by Randall M. German, pp. 568. ISBN 0-471-05786-X. Wiley-VCH, January 1996. 1996, 1.
9. S. Tawfick, X. P. Deng, A. J. Hart, J. Lahann. Nanocomposite microstructures with tunable mechanical and chemical properties. *PCCP*, **12**, 4446-4451 (2010).
10. M. F. L. De Volder, S. H. Tawfick, R. H. Baughman, A. J. Hart. Carbon nanotubes: present and future commercial applications. *Science* **339**, 535-539 (2013).
11. M. R. Maschmann, G. J. Ehlert, S. J. Park, D. Mollenhauer, B. Maruyama, A. J. Hart, J. W. Baur. Visualizing strain evolution and coordinated buckling within CNT arrays by in situ digital image correlation. *Adv. Funct. Mater.* **22**, 4686-4695 (2012).



12. M. R. Maschmann, Q. Zhang, R. Wheeler, F. Du, L. Dai, J. Baur. In situ SEM observation of column-like and foam-like CNT array nanoindentation. *ACS Appl. Mater. Interfaces* **3**, 648-653 (2011).
13. A. Y. Cao, P. L. Dickrell, W. G. Sawyer, M. N. Ghasemi-Nejhad, P. M. Ajayan. Super-compressible foamlike carbon nanotube films. *Science* **310**, 1307-1310 (2005).
14. S. Vaddiraju, H. I. Cebeci, K. K. Gleason, B. L. Wardle. Hierarchical Multifunctional Composites by Conformally Coating Aligned Carbon Nanotube Arrays with Conducting Polymer. *ACS Appl. Mater. Interfaces* **1**, 2565-2572 (2010); O. Hildreth, B. Cola, S. Graham, C. P. Wong. Conformally coating vertically aligned carbon nanotube arrays using thermal decomposition of iron pentacarbonyl. *J. Vac. Sci. Technol., B* **30**, 03D101 (2012); C. F. Herrmann, F. H. Fabreguette, D. S. Finch, R. Geiss, S. M. George. Multilayer and functional coatings on carbon nanotubes using atomic layer deposition. *Appl. Phys. Lett.* **87**, 123110 (2005).
15. A. J. Hart, A. H. Slocum. Rapid growth and flow-mediated nucleation of millimeter-scale aligned carbon nanotube structures from a thin-film catalyst. *J. Phys. Chem. B* **110**, 8250-8257 (2006).
16. C. K. Devine, C. J. Oldham, J. S. Jur, B. Gong, G. N. Parsons. Fiber containment for improved laboratory handling and uniform nanocoating of milligram quantities of carbon nanotubes by atomic layer deposition. *Langmuir* **27**, 14497-14507 (2011).
17. D. B. Farmer, R. G. Gordon. Atomic layer deposition on suspended single-walled carbon nanotubes via gas-phase noncovalent functionalization. *Nano Lett.* **6**, 699-703 (2006).
18. B. N. Wang, R. D. Bennett, E. Verploegen, A. J. Hart, R. E. Cohen. Quantitative characterization of the morphology of multiwall carbon nanotube films by small-angle X-ray scattering. *J. Phys. Chem. C* **111**, 5859-5865 (2007); M. Bedewy, E. Meshot, H. Guo, E. Verploegen, W. Lu, A. Hart. Collective mechanism for the evolution and self-termination of vertically aligned carbon nanotube growth. *J. Phys. Chem. C* **113**, 20576-20582 (2009); E. R. Meshot, D. L. Plata, S. Tawfick, Y. Y. Zhang, E. A. Verploegen, A. J. Hart. Engineering Vertically Aligned Carbon Nanotube Growth by Decoupled Thermal Treatment of Precursor and Catalyst. *ACS Nano* **3**, 2477-2486 (2009).
19. M. Bedewy, E. R. Meshot, M. J. Reinker, A. J. Hart. Population growth dynamics of carbon nanotubes. *ACS Nano* **5**, 8974-8989 (2011).
20. S. J. Park, A. J. Schmidt, M. Bedewy, A. John Hart. Measurement of carbon nanotube microstructure relative density by optical attenuation and observation of size-dependent variations. *PCCP* **15**, 11511-11519 (2013); M. Bedewy, B. Farmer, J. Hart, In preparation.

21. M. R. Maschmann, G. J. Ehlert, S. J. Park, D. Mollenhauer, B. Maruyama, A. J. Hart, J. W. Baur. Visualizing strain evolution and coordinated buckling within CNT arrays by in situ digital image correlation. *Adv. Funct. Mater.* **22**, 4686-4695 (2012).
22. B. I. Yakobson, C. J. Brabec, J. Bernholc. Nanomechanics of carbon tubes: Instabilities beyond linear response. *Phys. Rev. Lett.* **76**, 2511-2514 (1996); A. Pantano, D. M. Parks, M. C. Boyce. Mechanics of deformation of single- and multi-wall carbon nanotubes. *J. Mech. Phys. Solids* **52**, 789-821 (2004).
23. E. R. Meshot, M. Bedewy, K. M. Lyons, A. R. Woll, K. A. Juggernaut, S. Tawfick, A. J. Hart. Measuring the lengthening kinetics of aligned nanostructures by spatiotemporal correlation of height and orientation. *Nanoscale* **2**, 896-900 (2010).
24. M. M. J. Treacy, T. W. Ebbesen, J. M. Gibson. Exceptionally high Young's modulus observed for individual carbon nanotubes. *Nature* **381**, 678-680 (1996).
25. M. K. Tripp, C. Stampfer, D. C. Miller, T. Helbling, C. F. Hermann, C. Hierold, K. Gall, S. M. George, V. M. Bright. The mechanical properties of atomic layer deposited alumina for use in micro- and nano-electromechanical systems. *Sens. Actuators, A* **130**, 419-429 (2006).
26. E. Andrews, W. Sanders, L. J. Gibson. Compressive and tensile behaviour of aluminum foams. *Mater. Sci. Eng., A* **270**, 113-124 (1999).
27. H. Cebeci, R. G. de Villoria, A. J. Hart, B. L. Wardle. Multifunctional properties of high volume fraction aligned carbon nanotube polymer composites with controlled morphology. *Compos. Sci. Technol.* **69**, 2649-2656 (2009).
28. L. J. Gibson, M. F. Ashby. The mechanics of 3-dimensional cellular materials. *Proc. R. Soc. London, Ser. A* **382**, 43 (1982).
29. In [http://www.hexcel.com/Resources/DataSheets/Brochure-Data-Sheets/Honeycomb\\_Attributes\\_and\\_Properties.pdf](http://www.hexcel.com/Resources/DataSheets/Brochure-Data-Sheets/Honeycomb_Attributes_and_Properties.pdf).
30. M. A. Worsley, S. O. Kucheyev, J. H. Satcher, Jr., A. V. Hamza, T. F. Baumann. Mechanically robust and electrically conductive carbon nanotube foams. *Appl. Phys. Lett.* **94**, 073115 (2009).
31. J. Zou, J. Liu, A. S. Karakoti, A. Kumar, D. Joung, Q. Li, S. I. Khondaker, S. Seal, L. Zhai. Ultralight multiwalled carbon nanotube aerogel. *ACS Nano* **4**, 7293-7302 (2010).
32. T. M. Tillotson, L. W. Hrubesh. Transparent ultralow-density silica aerogels prepared by a 2-step sol-gel process. *J. Non-Cryst. Solids* **145**, 44-50 (1992).

33. N. Yamamoto, A. J. Hart, E. J. Garcia, S. S. Wicks, H. M. Duong, A. H. Slocum, B. L. Wardle. High-yield growth and morphology control of aligned carbon nanotubes on ceramic fibers for multifunctional enhancement of structural composites. *Carbon* **47**, 551-560 (2009).
34. E. S. Polsen, A. G. Stevens, A. J. Hart. Laser printing of nanoparticle toner enables digital control of micropatterned carbon nanotube growth. *ACS Appl. Mater. Interfaces* **5**, 3656-3662 (2013).
35. G. N. Parsons, S. M. George, M. Knez. Progress and future directions for atomic layer deposition and ALD-based chemistry. *MRS Bull.* **36**, 865-871 (2011).

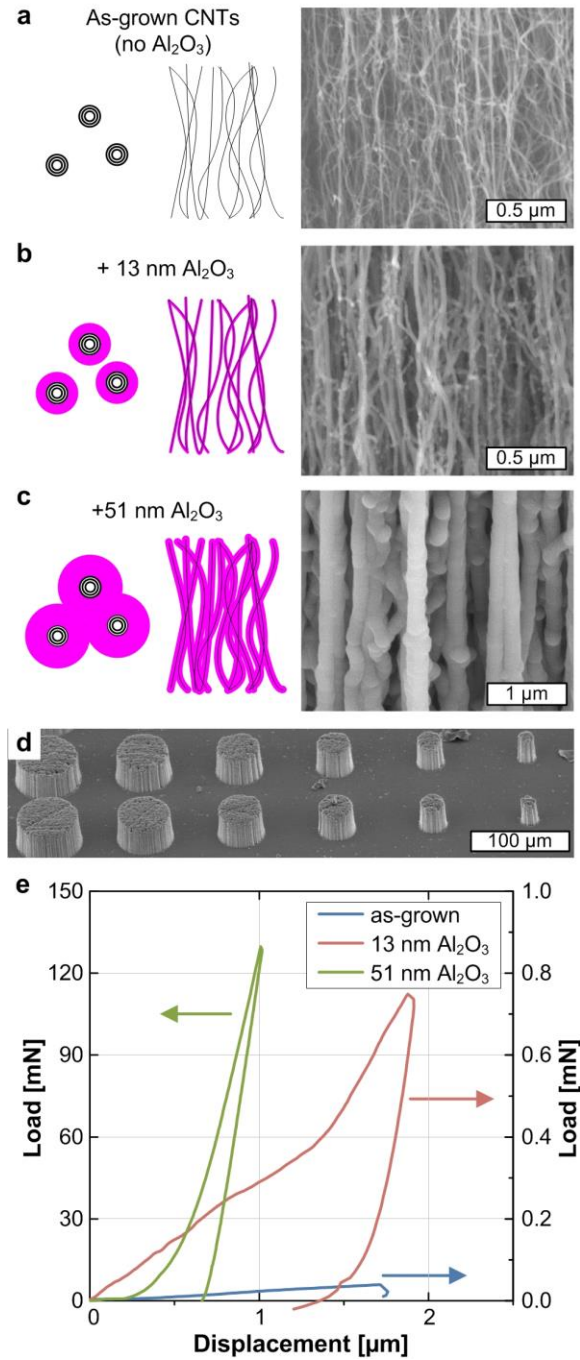


Figure 1. Morphology, structure and compression testing of Al<sub>2</sub>O<sub>3</sub>-carbon nanotube (CNT) foam. (a) Schematic and scanning electron microscope (SEM) image of as-grown vertically aligned CNTs ("forest"). CNT forest conformally coated with (b) 13 nm thick and (c) 51 nm thick Al<sub>2</sub>O<sub>3</sub> by atomic layer deposition (ALD). (d) Row of Al<sub>2</sub>O<sub>3</sub>/CNT micropillars fabricated for micro-compression testing. (e) Load-displacement measurement of micropillars (D = 30  $\mu\text{m}$ ), having nanoscale morphology as shown in (a-c).

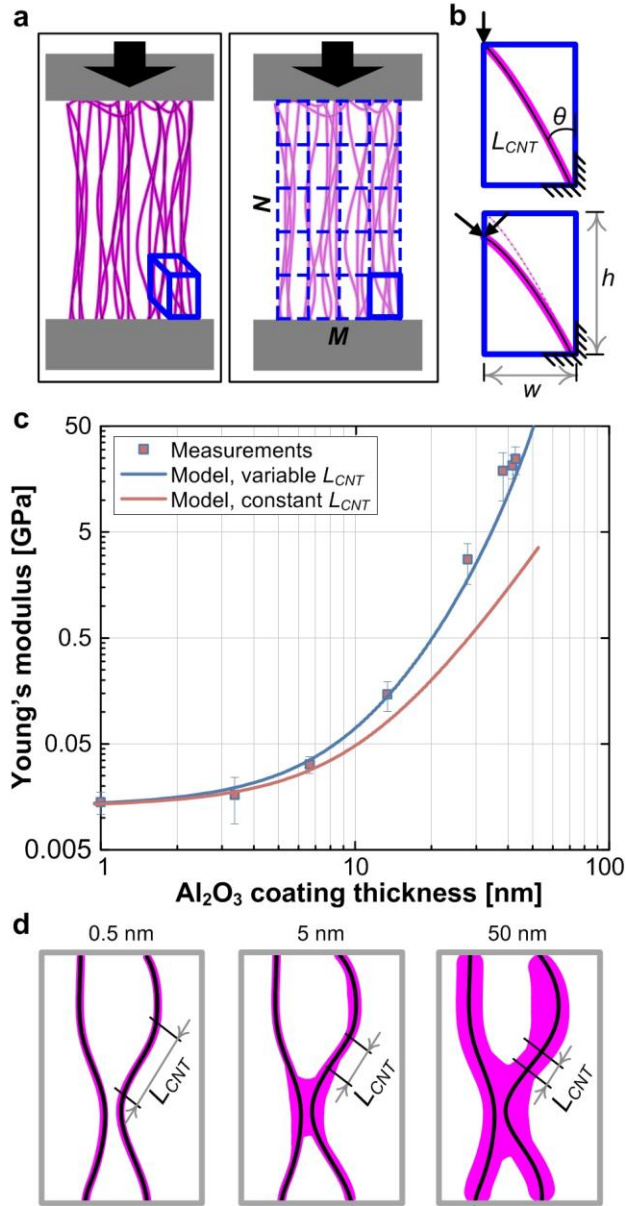


Figure 2. Unit cell model to predict compressive stiffness of Al<sub>2</sub>O<sub>3</sub>-CNT foams, based on bending deformation of angled core-shell beams. (a) Schematic of composite micropillar, and representative decomposition into  $N \times M$  unit cells. (b) Schematic of an individual unit cell showing a CNT beam in bending, with load decomposed into parallel and perpendicular components. (c) Comparison of measurements and model of the scaling of Young's modulus with the Al<sub>2</sub>O<sub>3</sub> coating thickness. (d) Schematics of the evolution of coating morphology, indicating reduction of the characteristic beam length which modifies the effective unit cell geometry.

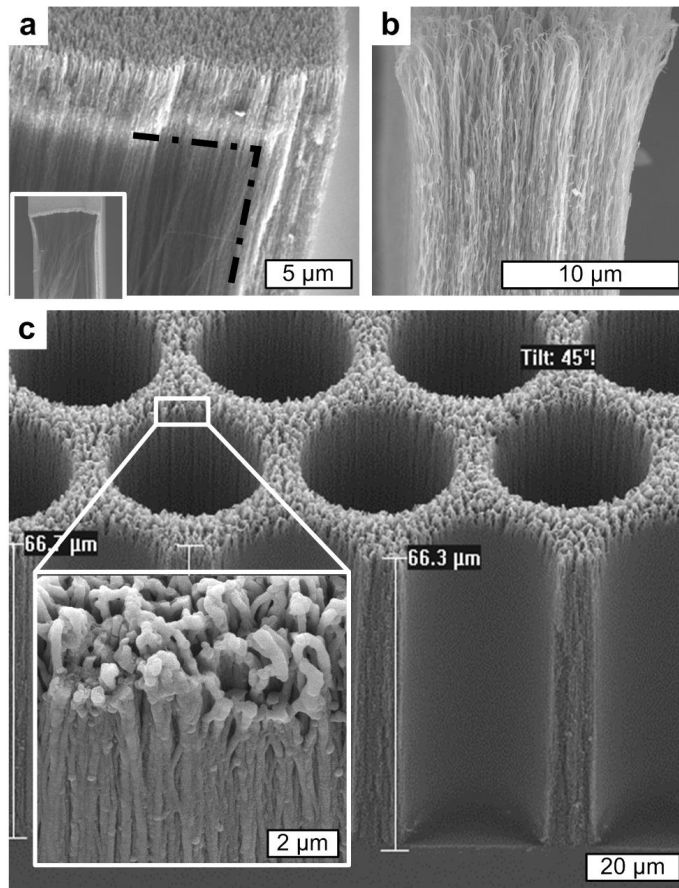


Figure 3. Penetration depth and hierarchical design of  $\text{Al}_2\text{O}_3$ -CNT composite films. (a) Cross section SEM of cleaved microwall (100  $\mu\text{m}$  width) showing the coating penetration depth (bright areas) from the top and the sides of the micropillar. (b) Cross section SEM of cleaved microwall (10  $\mu\text{m}$  width) showing uniform coating throughout the thickness. (c) Hierarchical honeycomb pattern with 10  $\mu\text{m}$  wall thickness designed to achieve uniform scaling of ALD coating over large areas.

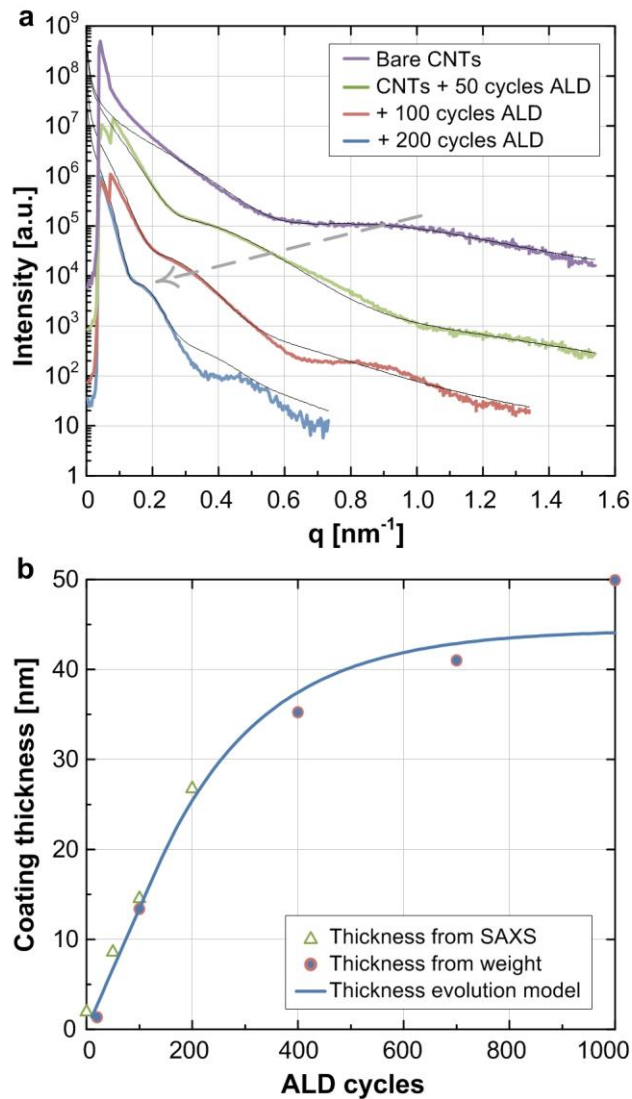


Figure 4. Characterization of core-shell CNT- $\text{Al}_2\text{O}_3$  morphology by Small Angle X-ray Scattering (SAXS) spectra of “honeycomb” pattern films. (a) I-q curves obtained from integration of SAXS images, showing evolution of primary scattering peak corresponding to population of cylindrical nanostructures. (b)  $\text{Al}_2\text{O}_3$  coating thickness obtained by fitting SAXS data with mathematical model, compared to measurements derived from weight change of each sample after ALD. Curve fit to (b) represents diffusion-limited infiltration of the CNT forest by the ALD coating precursors.

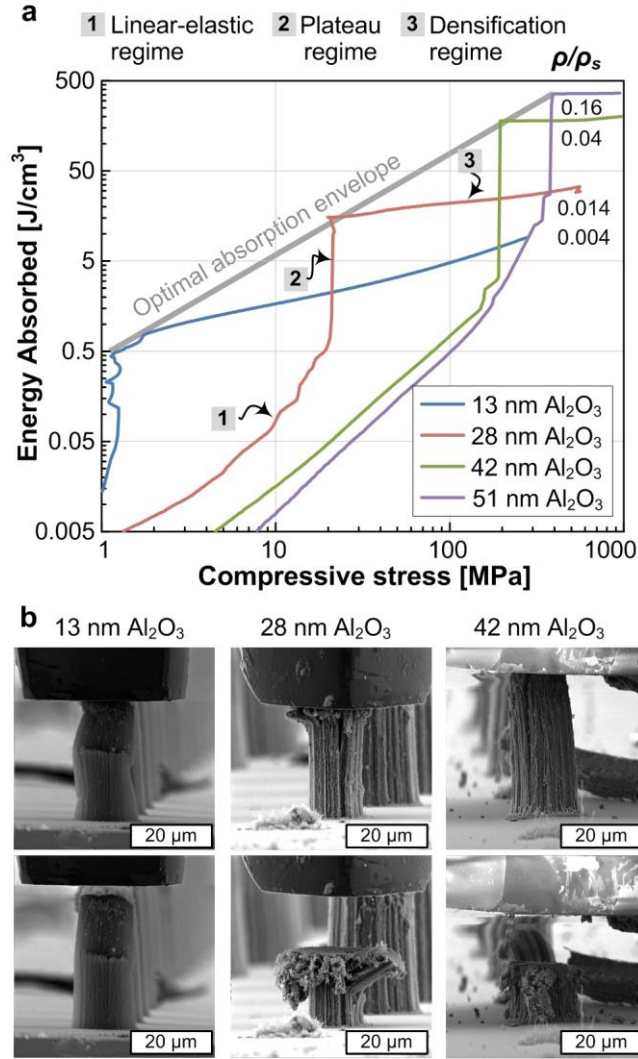


Figure 5. Toughness of  $\text{Al}_2\text{O}_3$ -CNT foams. (a) Strain energy absorbed versus stress for micropillars with different  $\text{Al}_2\text{O}_3$  coating thickness, showing the transition from linear elastic compression to the plateau (increase in strain without increase in stress) and the densification regimes (increase in stress without increase in strain). (b) SEM images from *in situ* compression testing showing the failure modes for coated CNT pillars at high strains: buckling for 13 nm thick coatings and cracking for 28 and 42 nm thick coatings. Top row shows micropillars during compression, and bottom row shows the same respective test after unloading.



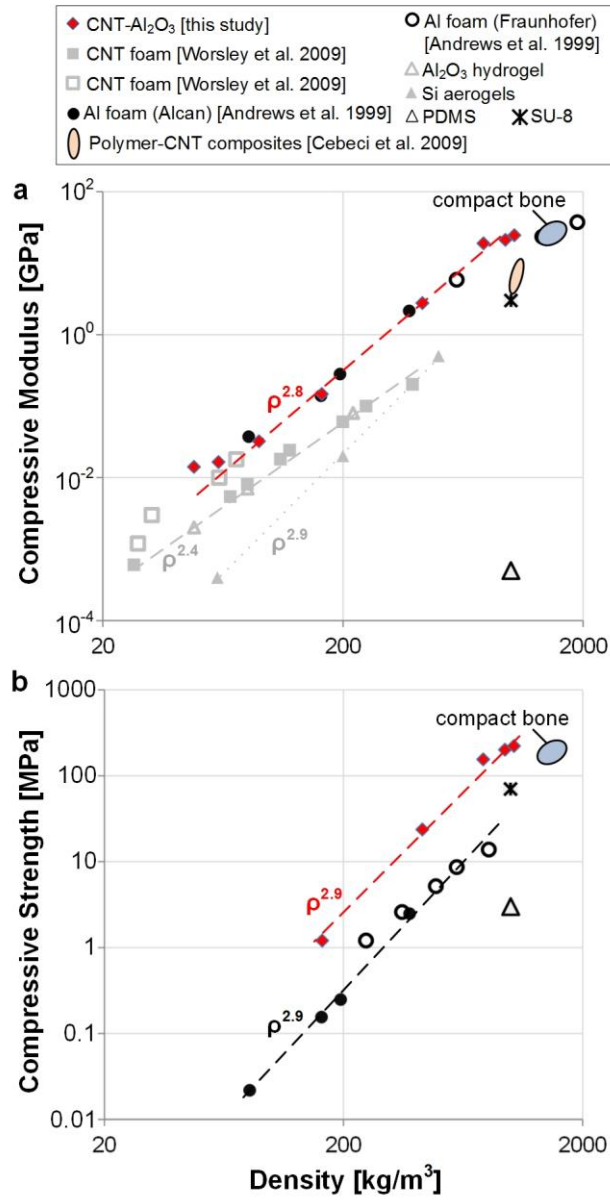


Figure 6. Measured power-law relationship between bulk density and compressive (a) Young's modulus and (b) strength of the Al<sub>2</sub>O<sub>3</sub>-CNT foams, compared to benchmark published and commercially available materials.

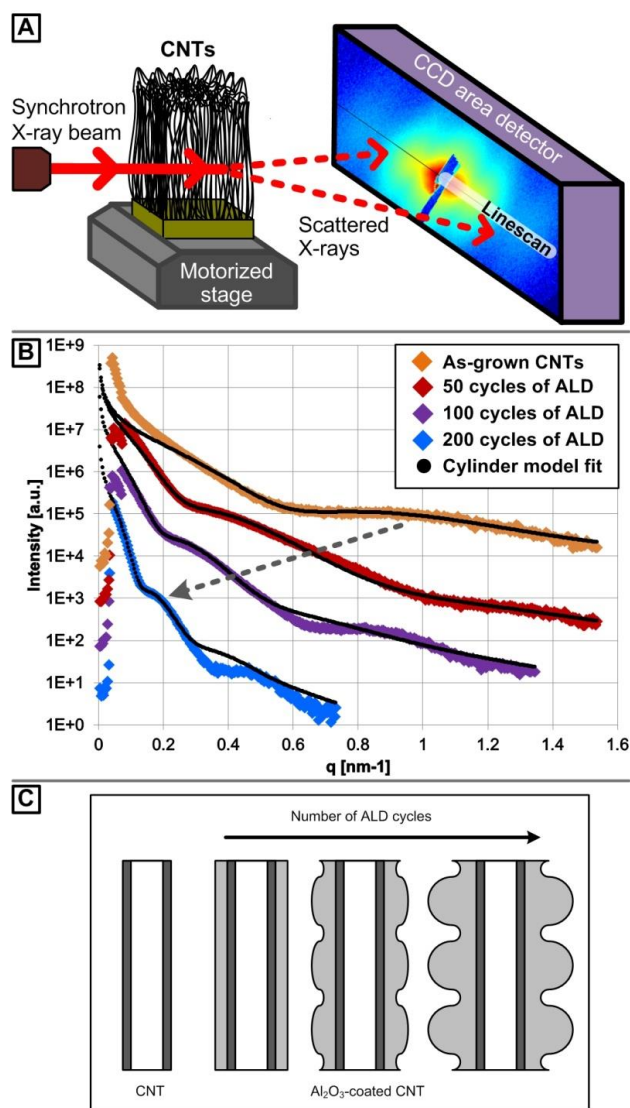


Figure S1. SAXS characterization of Al<sub>2</sub>O<sub>3</sub> coating thickness evolution. (a) Schematic of experimental setup for high energy transmission SAXS of vertically aligned CNT; (b) Line scans of scattering spectra having various number of ALD cycles, where arrow indicates the decrease in  $q$  with the increased number of cycles in addition to the appearance of a new peak at high  $q$  values; and (c) schematics qualitatively showing the evolution of the film thickness as well as the surface roughness of the CNT-Al<sub>2</sub>O<sub>3</sub> tubes.

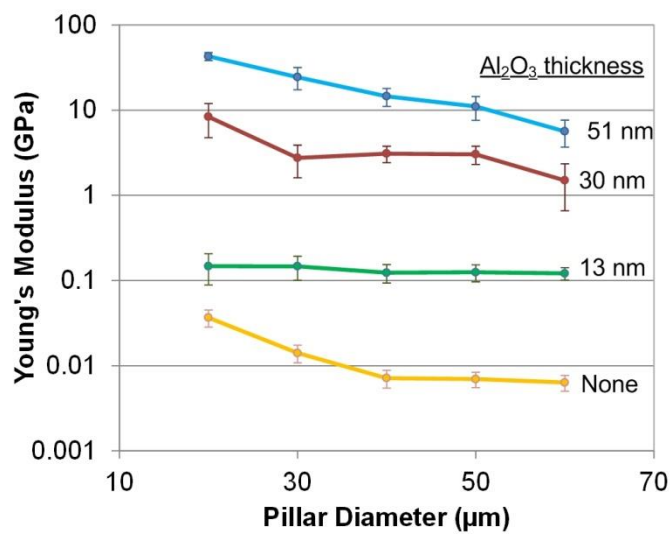


Figure S2. Measured Young's modulus (in compression) as versus micropillar diameter for bare CNTs, and CNTs coated with 13, 30, and 51 nm Al<sub>2</sub>O<sub>3</sub> by ALD.

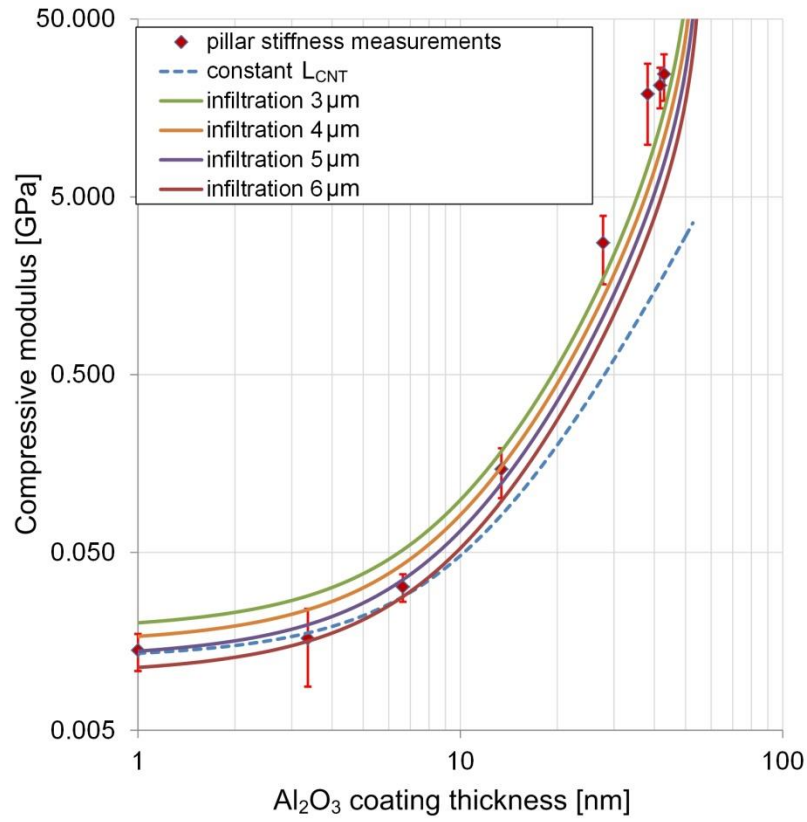


Figure S3. Plot showing the sensitivity of the model, used to predict Young's modulus, to the penetration depth of the ALD coating (hence changing the coated volume of the micropillar).

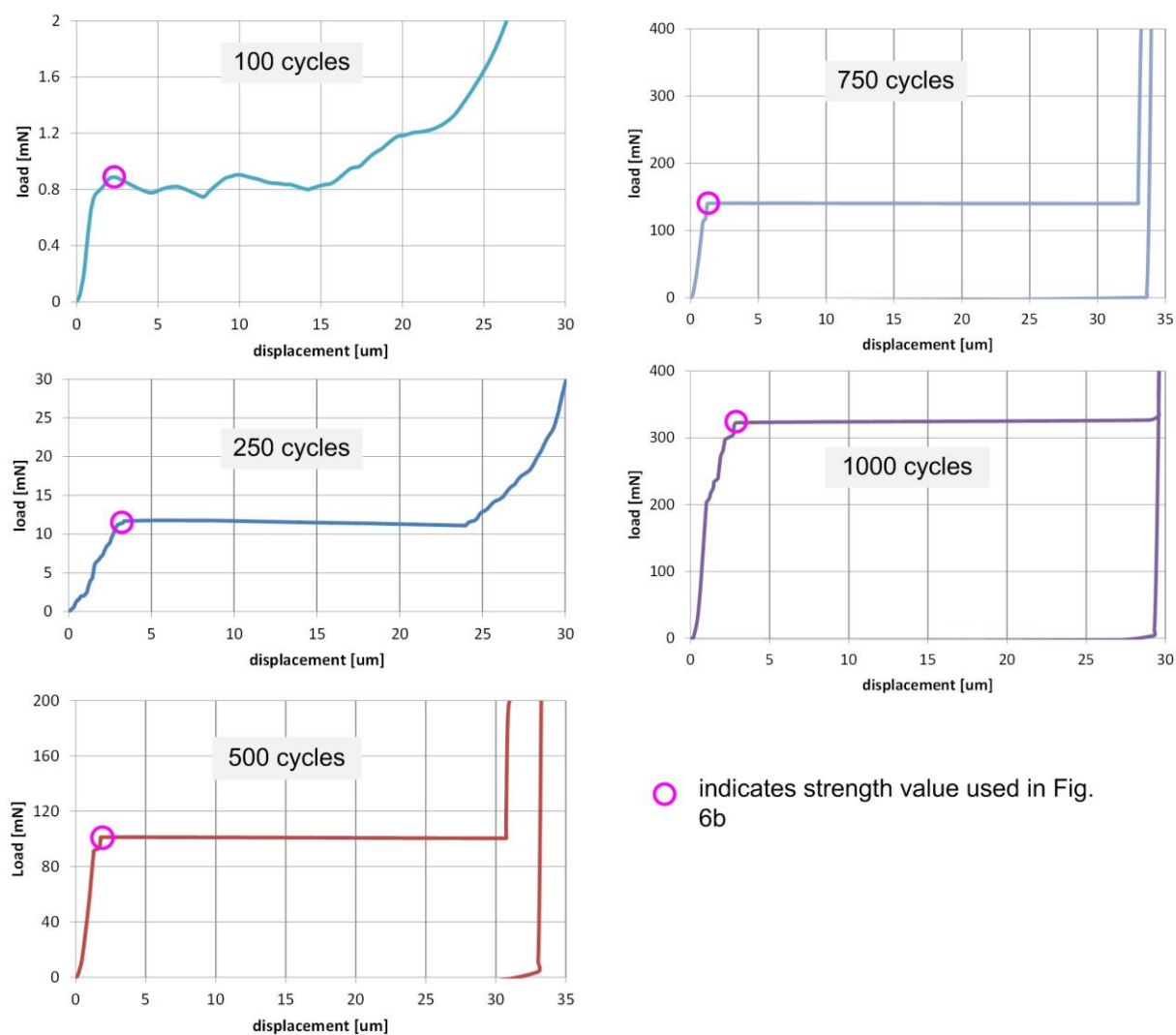


Figure S4. Load-displacement curves for  $\text{Al}_2\text{O}_3/\text{CNT}$  micropillars, with number of ALD cycles as noted. The circle superimposed on each curve indicates the strength value used to construct the strength-density relationship in Figure 6.

1.

**1. Report Type**

Final Report

**Primary Contact E-mail**

Contact email if there is a problem with the report.

ajhart@mit.edu

**Primary Contact Phone Number**

Contact phone number if there is a problem with the report

617.324.7022

**Organization / Institution name**

Massachusetts Institute of Technology

**Grant/Contract Title**

The full title of the funded effort.

Morphing Carbon Nanotube Microstructures

**Grant/Contract Number**

AFOSR assigned control number. It must begin with "FA9550" or "F49620" or "FA2386".

FA9550-11-1-0089

**Principal Investigator Name**

The full name of the principal investigator on the grant or contract.

Anastasios John Hart

**Program Manager**

The AFOSR Program Manager currently assigned to the award

Dr. Byung-Lip "Les" Lee

**Reporting Period Start Date**

05/01/2011

**Reporting Period End Date**

08/31/2014

**Abstract**

This AFOSR YIP Program sought to investigate the fabrication and properties of 3D "morphing" carbon nanotube (CNT) microstructures. It was proposed that morphing CNT microstructures would operate by swelling of an active material in a direction locally perpendicular to the CNTs. This shape change, in combination with the mechanical and electrical characteristics of the CNTs, could enable incorporation of intrinsic actuation and sensing behaviors in design of new structural materials and active surfaces. This final performance report, presented in four self-contained chapters, describes the major accomplishments of the AFOSR program. These include advances in the fabrication and mechanics of CNT microstructures, and demonstrations of novel composite materials and active materials based on composites of organized CNTs, polymers, and ceramics. Future work may focus on achieving extreme stimuli-responsive deformations using CNT-polymer and CNT-LCN systems, and enabling multifunctional surfaces combining the strain-dependent electrical properties of CNTs with their active response.

**Distribution Statement**

This is block 12 on the SF298 form.

### Explanation for Distribution Statement

If this is not approved for public release, please provide a short explanation. E.g., contains proprietary information.

### SF298 Form

Please attach your [SF298](#) form. A blank SF298 can be found [here](#). Please do not password protect or secure the PDF. The maximum file size for an SF298 is 50MB.

[AFD-070820-035.pdf](#)

**Upload the Report Document. File must be a PDF. Please do not password protect or secure the PDF. The maximum file size for the Report Document is 50MB.**

[Report-ALL-v01.pdf](#)

**Upload a Report Document, if any. The maximum file size for the Report Document is 50MB.**

### Archival Publications (published) during reporting period:

A. Brieland-Shoultz\*, S. Tawfick\*, S.J. Park\*, M. Bedewy, M.R. Maschmann, J. W. Baur, A.J. Hart. Scaling the stiffness, strength, and toughness of ceramic-coated nanotube foams into the structural regime. *Advanced Functional Materials*, 24(36):5728-5735, 2014. [<http://dx.doi.org/10.1002/adfm.201400851>]

M. De Volder\*, S.J. Park\*, S. Tawfick, A.J. Hart. Strain-engineered manufacturing of freeform carbon nanotube microstructures. *Nature Communications*, (5):4512, 2014. [<http://dx.doi.org/10.1038/ncomms5512>]

D. Copic, A.J. Hart. High-stroke actuation of aligned CNT-paraffin composite films. 19th International Conference on Composite Materials (ICCM), 2013.

D. Copic, A. Ya'akovovitz, A.J. Hart. Replica molding of liquid crystal polymer microstructures for active surfaces. 19th International Conference on Composite Materials (ICCM).

M.R. Maschmann, G. Ehlert, S.J. Park, D. Mollenhauer, B. Maryuama, A.J. Hart, J.W. Baur. Visualizing strain evolution and coordinated buckling in CNT arrays by in situ digital image correlation. *Advanced Functional Materials* 22:4686-4695, 2012.

M.R. Maschmann, G.J. Ehlert, S. Tawfick, A.J. Hart, J.W. Baur. Continuum analysis of carbon nanotube array buckling enabled by anisotropic elastic measurements and modeling. *Carbon*, 66:377-386, 2014. [<http://dx.doi.org/10.1016/j.carbon.2013.09.013>]

S. Tawfick, Z. Zhao, M.R. Maschmann, A. Brieland-Shoultz, M. De Volder, J.W. Baur, W. Lu, A.J. Hart. Mechanics of capillary forming of aligned carbon nanotube assemblies. *Langmuir* 29 (17): 5190–5198, 2013. [<http://dx.doi.org/10.1021/la4002219>]

### Changes in research objectives (if any):

None.

### Change in AFOSR Program Manager, if any:

None.

### Extensions granted or milestones slipped, if any:

The program was extended from the original end date until August 31, 2014.

### AFOSR LRIR Number

### LRIR Title

**Reporting Period**

**Laboratory Task Manager**

**Program Officer**

**Research Objectives**

**Technical Summary**

**Funding Summary by Cost Category (by FY, \$K)**

	Starting FY	FY+1	FY+2
Salary			
Equipment/Facilities			
Supplies			
Total			

**Report Document**

**Report Document - Text Analysis**

**Report Document - Text Analysis**

**Appendix Documents**

**2. Thank You**

**E-mail user**

Feb 06, 2015 20:02:55 Success: Email Sent to: ajhart@mit.edu